ABSTRACT

Title of Dissertation:	SPIN-PHOTON INTERFACE USING CHARGE TUNABLE QUANTUM DOTS
	Zhouchen Luo, Doctor of Philosophy, 2021
Dissertation directed by:	Professor Edo Waks Department of Electrical and Computer Engineering

The unconditional security of quantum networks and unparalleled acceleration of quantum algorithms enabled by "quantum computers" has motivated significant research across scientific communities. Among these different architectures to achieve such quantum information processing paradigms, a promising and straightforward proposal is the use of photons as flying qubits to transfer quantum information as well as local quantum memories to store and process quantum information. Toward this goal, it is very important to develop a type of quantum memory that can efficiently interface with photons while possessing good qubit properties, including a long coherence time and good scalability. To date, researchers have developed promising solid state quantum memory platforms, such as defects in diamond and other group IV compounds, rare earth ions hosted in various materials and self-assembled quantum dots. While each platform has its strengths and challenges, this thesis will focus on charge tunable InAs quantum dots grown inside a GaAs matrix that is doped into a PN

junction. Though not long after the first demonstration of optically active self-assembled quantum dots, researchers have already developed the idea to sandwich them inside a PN junction to tune their charge status. The spin manipulation in the strong coupling regime has been mostly using these dots without PN junction doping, which has resulted in limited dot-cavity cooperativity and spin lifetime due to electron tunneling.

In this thesis, I will first show the design, fabrication and characterization of several common photonic cavities, with their performance compared. Second I will show strong coupling between a negatively charged quantum dot and photonic crystal cavity, where the resonant cavity reflectivity is strongly dependent on the spin state. Third I will show that the electron spin lifetime (T1) can be significantly shortened by an off-resonant laser that reaches the device surface. While the exact reason for this undesired effect is not clear yet, we did observe the thickness of the electron tunnel barrier of the quantum dot wafer can result in distinct spin properties. I will present electron spin T1 characterization across several different quantum dot samples with different electron tunneling barrier thickness. Lastly, I will present coherent control of electron spin using picosecond laser pulse and sidebands of modulated continuous wave laser with limited spin rotation fidelity due to the off-resonant laser induced deterioration of the spin properties.

SPIN-PHOTON INTERFACE USING CHARGE TUNABLE QUANTUM DOTS

by

Zhouchen Luo

Dissertation submitted to the Faculty of the Graduate School of the
University of Maryland, College Park, in partial fulfillment
of the requirements for the degree of
Doctor of Philosophy
2021

Advisory Committee:
Professor Edo Waks, Chair
Steven Rolston, Dean's Representative
Professor Mario Dagenais
Professor Cheng Gong
Professor Thomas E. Murphy

Dedication

To my family and to us tiny human kind.

Acknowledgements

I want to first thank my advisor, Professor Edo Waks, for his guidance and generous support of my research through the past six years at Maryland. While he gave us enough freedom to carry out research and supported it with full strength, we could always get his opinion, suggestions and help when we had problems. He made it possible for us to try new ideas freely and bravely. Through those weekly meetings where we discussed exciting new ideas, I learned basic picture of this field and also his philosophy of tackling and handling problems. The longer I work with him, the more knowledge I realize he has.

I am grateful that my dissertation committee members, Professor Dagenais, Professor Murphy, Professor Gong and Professor Rolston, were willing to take the time to review my thesis and supervise my defense. Professor Dagenais and Professor Murphy also served in my proposal committee.

I owe a lot to Shuo Sun, who shuttled me during my beginning years in the lab. I learned most basic experimental techniques and theories from him. I want to acknowledge my close collaborator, colleague and friend in our group, Dr. Dima Farfurnik. I am really impressed by his fearless ideas, intelligence and diligence. We spent almost two years working closely on same projects. A lot of the spin exploration experiments of this dissertation were conducted together with him. He is a cheerleader of our research and is always brave enough to try new ideas and carries them out efficiently.

I want to thank our collaborators at the Naval Research Lab, Dr. Allan Bracker, Dr. Sam Carter and Dr. Dan Gammon, for their unique high-quality wafers. Those

wafers were the key to my research. We had many joint meetings to discuss our research progress, and their input and support were really valuable.

I also need to thank the staff of our nano fabrication center for their training and help using the semiconductor fabrication equipment. I especially want to thank Tom Loughran for his tireless help on fixing and maintaining the chlorine etcher. I also need to thank Dr. Juncun Rao and Dr. Sz-Chian Liou at the AIM lab for their training and help with the SEM. Also, I want to thank all IREAP staff who maintained and provided the basic environment of our research. Dr. Don Schmadel and Bryan Quinn helped a lot on our lab related issues. Nancy Boone handled all our procurement efficiently and flawlessly.

I want to thank all my fellow colleagues and friends, Tao Cai, Aziz Karashin, Dr. Chang-Min Lee, Dr. Robert Pettit, Dr. Kim Jehyung, Shahriar Aghael, Subhojit Dutta, Mustafa Buyukkaya, Zhili Yang, Sabyasachy Barik, Sam Harper, Uday Saha, Harjot Singh, Chang-Mu Han, Dr. Hamidreza Chalabi, Yu Shi, Yuqi Zhao and Xinyuan Zheng, for all those discussions and help, day and night, in and out of the lab. They make our lab a lovely place to stay.

Lastly, I thank my parents for their love and support.

I met a girl on campus whose name is Leanne. We have been together for four years now, though most of the time we were separated by the Pacific. From now on, we shall stay together both in real life and in this chapter.

Table of Contents

List of Tables

List of Figures

List of Abbreviations

QED Quantum Electrodynamics

Qubit Quantum Bit

QD Quantum Dot

PhC Photonic Crystal

InAs Indium Arsenide

GaAs Gallium Arsenide

InGaAs Indium Gallium Arsenide

InP Indium Phosphide

FDTD Finite-difference Time Domain

SPCM Single Photon Counting Module

LED Light Emitting Diode

PL Photoluminescence

SEM Scanning Electron Microscopy

EBL Electron Beam Lithography

ICP Induction Coupled Plasma

IPA Isopropyl alcohol

RF Radio Frequency

AWG Arbitrary Waveform Generator

FWHM Full Width Half Maximum

CCD Charge Coupled Device

EOM Electro-Optic Modulator

Chapter 1: Introduction

1.1 Overview

Future quantum networks[1,2] and distributed quantum computing[3] rely on quantum information and entanglement to be distributed among distant nodes. Photons are natural and ideal flying qubits that can be used to transfer quantum information and distribute entanglement[4,5]. Spins are pristine quantum memory that can be used to store and process quantum information. Effectively interfacing spin with a photon can be used to achieve basic building blocks of the above mentioned quantum information processing paradigm such as spin-mediated photon-photon interactions[6–8] for photonic quantum computation[6,9] and entanglement distribution.

Solid state spin systems can be easily integrated with various functional photonic devices[10,11] and have advantage of scalability compared to more isolated systems, like trapped ions and cold atoms. Electron or hole spins hosted in semiconductor self-assembled quantum dots[12–14] are one of the most promising solid states systems that have been found so far. On the one hand, it has been reported to have a spin lifetime (T1) of up to milliseconds[12,15] and coherence time of up to microseconds[16] under a finite external magnetic field (few Tesla). On the other hand, the spin ground states are connected to its excited states via optical transitions that can be utilized as a quantum light source.[17,18] So far, single photon sources that feature high quantum efficiency (> 90%), low impurity (< 0.01) and high indistinguishability (> 0.99) have been demonstrated using these opticallt active self-assembled quantum dots[19,20]. Other non-classical light states[21], such as cluster states[22] and GHZ states[23]

which are important for photonic quantum information processing could also be prepared using quantum dots.

Coupling such charged quantum dots to photonic crystal cavities enables strong spin−photon interfaces[7,24–30], where the spin state of the quantum dot can modulate the cavity reflectivity, allowing the spin to control the state of the reflected photons. Such interfaces are essential for solid-state quantum networks and photonic quantum computation, and have been proposed as a building block for applications like quantum phase gates[6] and quantum repeaters[31,32].

Several studies have demonstrated such strong spin-photon interfaces between the electron spin of a charged quantum dot and cavity[33–36], enabling optical nonlinearities such as Kerr rotations[35,37] and single-photon transistors.[33] These studies have relied on probabilistically charged quantum dots due to nearby impurities. However, this charging mechanism results in low charge stability due to carrier tunneling[36], causing poor spin initialization and qubit gate fidelity[33]. Alternatively, charge tunable devices,[38–40] which typically feature a p-i-n diode structure, can be used to control and stabilize the electron charging state in a quantum dot. This diode structure can also increase atom-cavity cooperativity (a figure of merit that describes the efficacy of the coherent energy exchange between the emitter and cavity field) by suppressing spectral wandering due to electric field noise induced by trapped surface charges.[41,42]

In this dissertation, we demonstrate a strong spin-photon interface using charge tunable quantum dot strongly coupled to an L3 photonic crystal cavity. We show a spin-cavity cooperativity with one order of magnitude improvement over previous

studies using probabilistically charged dots. In addition, we explored electron spin properties across multiple charge tunable quantum dots samples. Electron tunneling limited spin T1 lifetimes and laser-induced shortening of T1 was observed. We also demonstrated coherent rotation of these electron spins with picosecond laser. This dissertation research represents an important step towards understanding and utilizing electron spins in such charge tunable devices.

1.2 Charge-Tunable Self-assembled Quantum Dots

Self-assembled quantum dots[14] are nano-particles that are several to hundreds of nanometers in size. They are grown within a host material using molecular beam epitaxy (MBE) in Starnski-Krastanov (SK) mode.[43] Quantum dots are a 3D potential well that can host semiconductor particles such as electrons, holes, and excitons.[44] Because excitons can be created and combined in quantum dots (they are usually a direct band gap material), they are typically optically active and thus sometimes they are also called optically active quantum dot. Since the quantum confinement is so tight due to their small size, quantum dots can have quasi discrete energy levels just like real atoms. This is also the reason that quantum dots are called "artificial atoms". From this point of view, applications and experiments based on real atoms should be possible to implement on quantum dots, which is one of the main research paths in the quantum dots community.

Self-assembled quantum dots have counterparts in other forms, including colloidal[45] and gate-defined quantum dots.[46] Colloidal quantum dots are synthesized using chemical methods and have many variants of different compositions. Their

applications typically focus on generating classical and coherent light as optical emitters and laser gain media. Gate-defined dots are spatially defined by electrodes of micrometer size that are patterned on the surface of semiconductor wafers using standard lithography. Multiple electrodes on the sample surface create a 2D potential well with micrometer lateral size. The wafer itself is single crystal or compound since the potential well is defined by the electrodes and does not rely on the interface of different semiconductor materials. Therefore, gate-defined quantum dots are sometimes also called strain-free quantum dots. Gate-defined dot are one of the earliest and most popular platforms that researchers have used as quantum bits (qubits) for the purpose of quantum information processing.[47] They share a lot physical mechanisms and properties as self-assembled quantum dots in term of their solid-state environment[48–50]. While measurement methods of gate-defined dots are mainly using Radio Frequency (RF) technique, the measurement of self-assembled dots are primarily optical.

In this thesis, I will exclusively focus on self-assembled quantum dots, specifically InAs quantum dots grown in a GaAs matrix wafer that emits at a near infrared band (roughly between 900 nm and 1000 nm). The 900-1000 nm emission band is not ideal for low loss transmission through optical fibers. For this reason, InAs dots sandwiched in an indium phosphide (InP) matrix that emits at the telecom band is also under intense development.[51]

1.3 *Layered Structure*

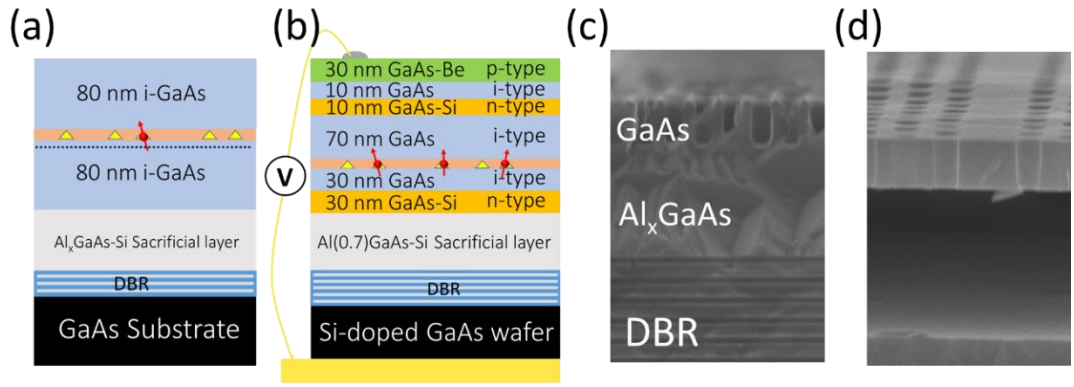

Figure 1.1 Layer structure of two typical types of self-assembled quantum dots used in this thesis. (a) Traditional quantum dots sample with a thin doping layer tens of nanometers below to increase the charging probability. The wafer we have doesn't have the n-type doping layer and its charging is thus created by nearby defects and need to be stabilized with above band lasers. (b) Charge tunable quantum dots buried in a p-i-n-i-n diode enabling its charging statusto be deterministically changed. (c) SEM of the cross section of a quantum dots wafer patterned with arrays of photonic crystal holes. The aluminum layer is not etched here. (d) SEM cross section of suspended photonic crystal cavity membrane. Image taken by Tao Cai of the Waks Group.

Figure 1.1 shows the layered structure of two typical types of quantum dot samples that are widely used. Figure 1.1(a) is a more traditional structure, in which a layer of InAs quantum dots (yellow triangles) on top of its wetting layer (orange layer, several nanometers thick) is sandwiched between intrinsic GaAs membrane, which typically has a thickness of several tens of nanometers. The InAs dots we use have a pyramidal shape with a lateral size of ~10 nanometers and height of several nanometers. The emerging positions of quantum dots during the growth are random but quasi uniform over the whole wafer. Typically 10 – 100 dots per micron square density is used with a good balance between device yielding and distinguishability. For the purpose of optical mode confinement, an aluminum gallium arsenide (AlGaAs) layer is usually grown below the GaAs to serve as a sacrificial layer to suspend the GaAs membrane. This is particularly important when photonic structures are patterned on the

GaAs membrane. Below the sacrificial layer, a distributed Bragg reflector (DBR) composed of tens of pairs of $\lambda/2$ mirrors is added to increase the upward light collection efficiency. Most of the dots in such structure are neutral. Some of them can be charged either with electrons or holes due to the natural defects of the wafer, but the charging probability is very low. To improve the charging probability, researchers usually add a doping layer around ten nanometers below the dots as carrier donors. Such sample structure cannot control the charging status of individual quantum dots and the charging stability is also poor.[52]

To deterministically control and stabilize the charging status of individual dot, researchers have developed PN junction type quantum dot wafers as shown in Figure 1.1(b). The PN junction or its variants can tune the relative position between the electron fermi surface and the quantum dots' energy band by varying the external gate voltage applied across the junction region, thus different number of electrons or holes can tunnel into the dot to form different charging states.[53,54]

Figure 1.1(c) and (d) are scanning electron microscopy (SEM) images of the cross-section of quantum dot wafers used in this thesis. The holes on the top surface are photonic crystals patterned by electron beam lithography (EBL) and induction coupled plasma (ICP) dry etching. The sacrificial layer in (d) is etched away by hydrofluoric acid (HF), leaving the photonic structure containing quantum dots suspended to better confine the optical mode.

1.4 Quantum Dot Energy Band

Figure 1.2 (a) is the energy band structure corresponding to the quantum dots wafer in Figure 1.1(a)[13,55,56]. Just like atoms, it also has discrete states with s- and p-

shape density functions[56,57]. Higher excited states are possible but not considered here. When an electron-hole pair or exciton is created in the GaAs bulk by light, it can migrate to the InAs quantum well, following the path of the wetting layer, p-shell state and s-shell state. The timescale moving from GaAs to InAs is reported to be around nanosecond.[13] The decay from the p-shell to s-shell is relatively fast, on the order of picosecond, accompanied with the release of phonons. The lifetime of the s-shell state is on the order of one nanosecond, allowing those dots to emit single photons on the GHz regime.[24]

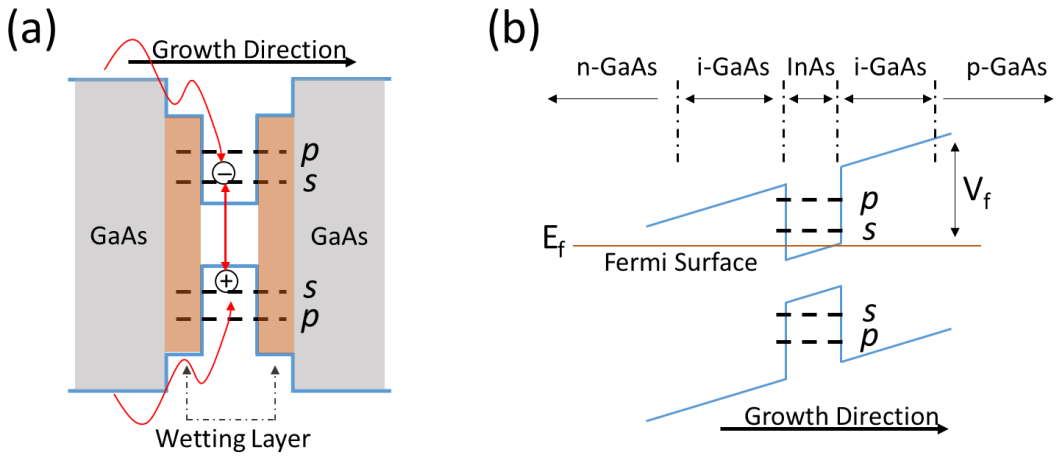

Figure 1.2 Energy band corresponding to the two types of quantum dot samples shown in Figure 1.1 respectively. (a) Energy band of quantum dot without p- or n- type doping. (b) Energy band of an InAs quantum dot sandwiched in a GaAs p-i-n diode. The energy band is tilt along the growth direction by the built-in electrical field and externally applied gate voltage. The wetting layer is omitted here for simplicity.

Figure 1.2 (b) is the energy band structure corresponding to the quantum dots wafer in Figure 1.1(b). When the GaAs membrane is doped into a PN junction or its variants, the energy band is tilted by the overall electrical field that the dots feel. By changing the external gate voltage across the PN diode, the relative distance between the quantum dots' electronic states and electron fermi surface can be tuned. Thus, individual electrons can tunnel in and out of the quantum dots depending on the gate

voltage,[56] allowing the number of extra electrons inside the quantum dots to be controlled.

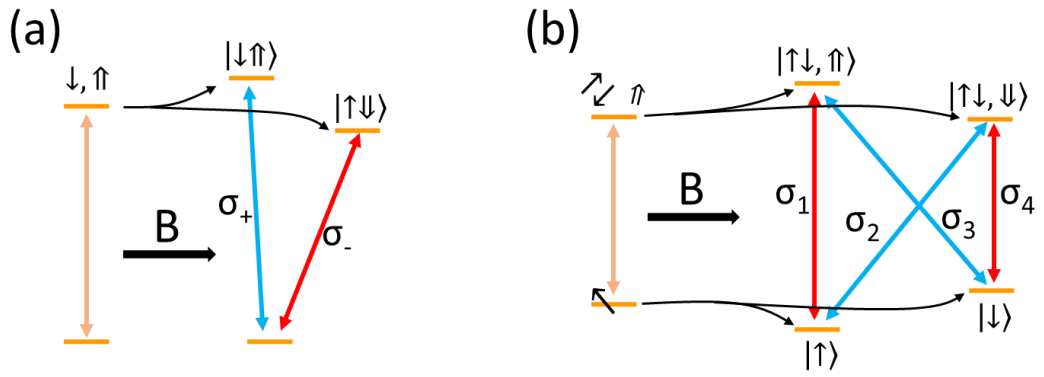

Figure 1.3 Energy level of quantum dots. (a) Energy level of a neutral quantum dot with (left) and without (right) an external magnetic field. (b) Energy level of a quantum dot charged with one electron with (left) and without (right) an external magnetic field.

When we only consider the lowest excited state of quantum dots (s-shell), which is usually enough to capture the most important physics, neutral quantum dots can be simplified as a two level system (TLS), as the left half of Figure 1.3 (a) shows. Its excited state is an electron-hole pair in the s-shell and its ground state is empty. The excited state and ground state is linked by an optical transition. When an external magnetic field is applied across dots, the excited state splits into two states with opposite spin projection along the direction of the magnetic field. The ground state is now connected to two excited states through two opposite circularly polarized optical transitions following spin conservation. When the dot is negatively charged with one electron, the energy level diagram is as shown in Figure 1.3 (b). When a magnetic field is applied, both ground and excited state degeneracy is lifted, forming four optical transitions.[55] When the direction of the magnetic field is aligned with the wafer growth direction (Z axis), which is the so-called Faraday configuration, only σ_1 and σ_4 are optically allowed with circular polarization due to spin conservation. While σ_2 and σ_3

are forbidden transitions in principle, they are weakly allowed with a dipole strength one or two orders smaller than the other two transitions due to heavy and light hole mixing in GaAs.[55] If the direction of the magnetic field is perpendicular to the wafer growth direction, which is called the Voigt configuration, all of the four transitions are optically allowed and are linearly polarized. In particular, the polarization of σ_1 and σ_4 are perpendicular to that of the other two.

1.5 Optical Properties

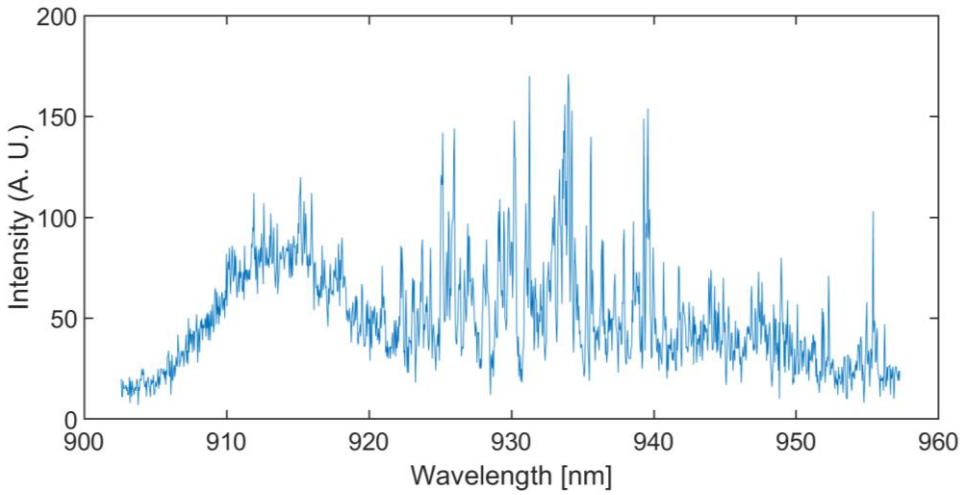

Figure 1.4 Photoluminescence of bulk quantum dots pumped by an above band laser around 890 nm. The sample were kept in a 4 Kelvin cryostat and measured at 0 Tesla.

Self-assembled quantum dots are by far the best quantum emitter people have found. They can emit single photons at the GHz level with more than 90% quantum efficiency. Combined with their simple integration with various photonic structures, single photon source with over 50% collection efficiency has been demonstrated,[19] making it the brightest single photon emitter platform. Additionally, researchers have shown transform limit linewidth down to 1 μeV in bulk quantum dot samples.[58,59] Though surface charge states and charge noise created by etched surfaces can broaden the emission linewidth, below 1 GHz linewidth has been reported by many groups.[58–

[60] More importantly, over 99.9% single photon purity and over 99% single photon indistinguishability has been reported using InAs quantum dots, making them undoubtedly the best quantum source so far. [19,20]

Figure 1.4 shows the typical above-band photoluminescence spectrum of bulk InAs quantum dots. Since the size of the laser spot focus on the sample surface is on the order of micrometer, several tens of quantum dots can be excited simultaneously. Each peak on the spectrum is emitted from a single quantum dot. Dots on the same wafer have slightly different physical size and local environments, such as strain, so their emission spectra have large inhomogeneous broadening, typically around several tens of nanometers. This is one of the disadvantages and challenges when trying to scale quantum optical devices based on self-assembled quantum dots. Another challenge applying these dots in real life is their location on the wafer is somewhat random, which obscures their on chip scalability. Several techniques have been developed to circumvent this problem, like site-controlled growth,[61] on-site lithography[62] and hybrid integration using the pick-place technique.[63]

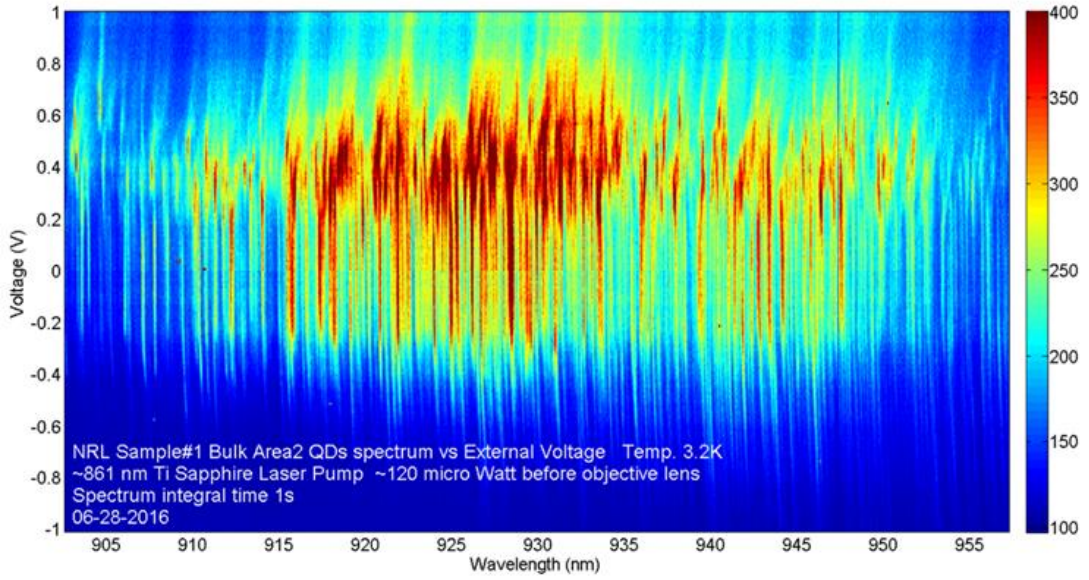

Figure 1.5 Photoluminescence of an early charge tunable quantum dots sample at different gate voltages. The color scale bar represents the intensity of the spectrum.

Figure 1.5 shows a common bias map of a charge tunable quantum dot sample grown by the Naval Research Lab. The photoluminescence at different gate voltage applied across the sample is recorded and then plotted in a 2D map form. Each emission line can only exist at a certain voltage range corresponding to one charging state of a single dot. The emission wavelengths of different charging states of a single dot are distinct from each other, typically separated by 0.1 to 10 nanometers. Each single line in Figure 1.5 represents the emission line of one charging state of a single dot. When the gate voltage is scanned across its multiple charging state, its emission wavelength jumps.

1.6 Spin Properties

When using an electron spin for the purpose of quantum information processing, two key figures of merit are spin's lifetime and coherence time. The spin

lifetime is also called the T1 time. Self-assembled InGaAs quantum dots have been reported to have T1 lifetimes ranging from nanoseconds to milliseconds,[12,15,64–71] and a coherence time (T2*) of several nanoseconds to microseconds.[16,48,52,72] Since the electron spin of self-assembled quantum dots exists in a solid-state environment, deterioration of its spin properties is quite common due to the interaction with reservoir like phonons and surrounding nuclei spins. We will cover the spin properties of our sample in detail in the following chapters.

1.7 Comparison with other Solid State Spin Systems

Compared with two other popular solid state spin systems, defect in diamonds[73] and rare earth ions,[74,75] self-assembled quantum dots are superior in terms of optical properties but fall short in regarding to spin properties. The small optical dipole strength of rare earth ions and diamond defects makes it difficult to achieve strong light-matter interactions. Their integration with various photonic structures is also not easy due to fabrication difficulties. Ions typically have very long lifetime, making them undesirable as high bandwidth quantum emitters. On the other hand, ions and diamond defects have shown very long spin lifetimes and coherence times. Up to hour long spin T1 and up to minutes of T2* coherence time have been reported in ion systems. Meanwhile up to minutes of T1 time and up to seconds of T2* coherence time have also been reported in diamond systems. Also, both ions and defects in diamond are site controllable as they are usually implanted via focus ion beams, making them preferable for scalability. Additionally, ions and diamond spins usually have very small inhomogeneous broadening.

While each system has its own advantages and challenges, hybrid devices take best of each world is a good solution. Since the research in this quantum engineering community is still undergoing rapid development, new spin platforms may emerge in the future.

1.8 Cavity Quantum Electrodynamics

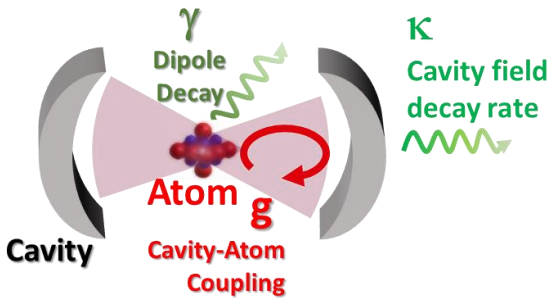

Figure 1.6 Schematic drawing of a cavity QED system composed of an atom and an optical cavity. The optical cavity is formed by two mirrors that are highly reflective. The atom is put inside the cavity with its emission field overlapping with the cavity modes.

Figure 1.6 is a schematic picture of a classic cavity quantum electrodynamics (QED) model. When an atom is placed in an optical cavity, its state density is modified by the coupling between its emission field and cavity mode, which is the so called Purcell effect. The coupling strength g can be quantified by the overlap between the atom emission field and cavity field. The optical cavity can be simplified as two highly reflective mirrors between which photons can be trapped with some lifetime due to the reflection of the mirror. The decay rate of light escaping the cavity can be described by cavity loss rate κ. Additionally, the atom's optical transition has its limited lifetime ϒ. When the coupling strength between the atom and cavity is larger than their own decay rates, hybridization of the modes of these two quantum systems (atom and cavity mode) occurs and forms two new modes with components from each individual system, which

is the so-called polaritons[76,77]. Since the coupling between the atom and cavity is larger than their own decay rates, coherent energy transfer can happen between atom and cavity before the light eventually leaks out of the cavity. This scenario is also called the strong coupling regime. Such cavity system is a generalized way to enhance light-matter interactions since photons will travel back and forth inside the cavity, during which it can interact with the atom more times. The atom in Figure 1.6 can be extended to many optical emitters including quantum dots, ions, and diamond color centers. Additionally, the optical cavity can take many forms.

1.9 Thesis Outline

In following chapters, I will describe in detail how I achieve strong a spin-photon interface using charge tunable quantum dots coupled to photonic structures. Additionally, I will discuss how we characterize the spin properties of the electron spins confined in those devices. Specifically, in Chapter 2, I will describe the design, fabrication and comparison of several photonic cavities I used during my Ph.D. research. In Chapter 3, I will demonstrate how to achieve strong coupling between charge tunable quantum dots and photonic crystal cavities. Additionally, I will show the statistical T1 measurement of electron spin across different wafers and how the T1 can be shortened by the laser reaching the sample surface. In Chapter Four, I will show the coherent manipulation of electron spin using picosecond laser and modulated continuous wave (CW) laser. Finally, in Chapter Five, I will give a conclusion of this dissertation research and an outlook of future experiments. Measurement setup and fabrication method are described in Appendix A and Appendix B respectively.

Chapter 2: Photonic Cavities

2.1 Chapter Introduction

In this Chapter, I will present several designs of photonic cavities I used in this dissertation research, specifically L3 (Linear three) photonic crystal cavity[78] (PhC), directional cavity[79], H1 PhC[80] and bullseye cavity[81,82]. All of them belong to the category of so called photonic crystal cavity except bullseye cavity.

The integration of quantum emitters with photonic cavities mainly has two purposes. One is to enhance the excitation and collection efficiency from the emitter through the redirection of light propagation via optical structures and the modification of emitter's lifetime via Purcell effect. The second purpose is to exploit the cavity QED effect, especially in the high cooperativity and strong coupling regime, where the cavity reflectivity can be modulated by the coupling between the cavity and atom. To fulfill these two goals, cavities with high quality factor (high Q), small mode volume and Gaussian shape far field emission patterned are preferred.

I will explain the design and measurement of one type of cavities in each sub chapter.

2.2 M1 mode of L3 Photonic Crystal Cavity

Photonic crystal cavity is a kind of nano-photonic cavity, featuring arrays of repetitive structures like real crystals. Its functioning idea was triggered by its counterpart in solid states system, where the repetitive wave functions with phase shift of atom crystal form the energy band. Those cavities usually have very small optical

mode volume ~$(\lambda/n)^3$ and moderate quality factor (~10^4), thus is suitable for the purpose to achieve strong light matter interaction.

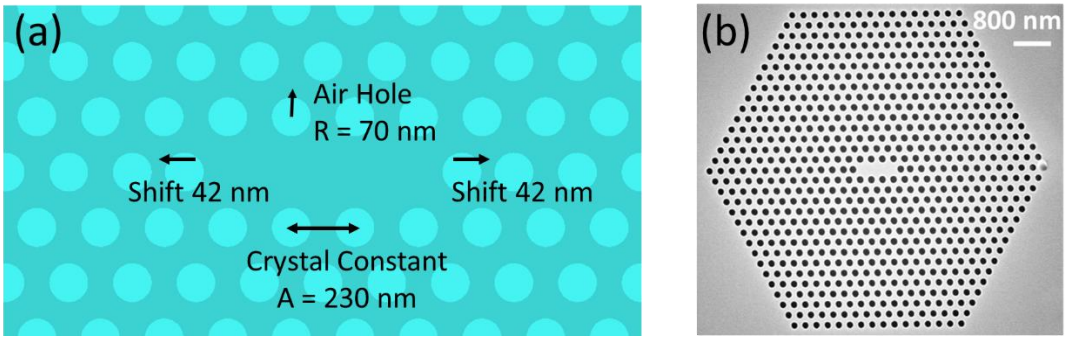

Figure 2.1 L3 Photonic Crystal Cavity. (a) Design of a L3 cavity with its resonance at around 934 nm. (b) The SEM image of fabricated L3 cavity on a GaAs slab with InAs quantum dots inside following the design in (a).

Figure 2.1 shows the design of L3 cavity[78] we used for InAs quantum dots. In the middle of the air hole lattice, three air holes are taken away to form the cavity region, which is the reason that it is called Linear Three (L3) cavity. The wavelength of its fundamental mode (M1 mode) is shifted to around 930 nm to match InAs quantum dots' emitting range from 900 nm to 960 nm (Figure 1.4 and Figure 1.5). The cavity's resonance wavelength is mainly dependent on the hole lattice constant, which is set to be 230 nm to achieve a cavity resonance of 930 nm. The nearest holes left and right to the cavity region is shifted to maximize its quality factor. The FDTD simulation shows a quality factor of ~120,000 with above design. More holes near cavity center can be included to be shifted around to increase the cavity quality factor, but the gain is not much. The radius of the air hole will also affect the cavity mode wavelength and quality factor, which is optimized to be 70 nm.

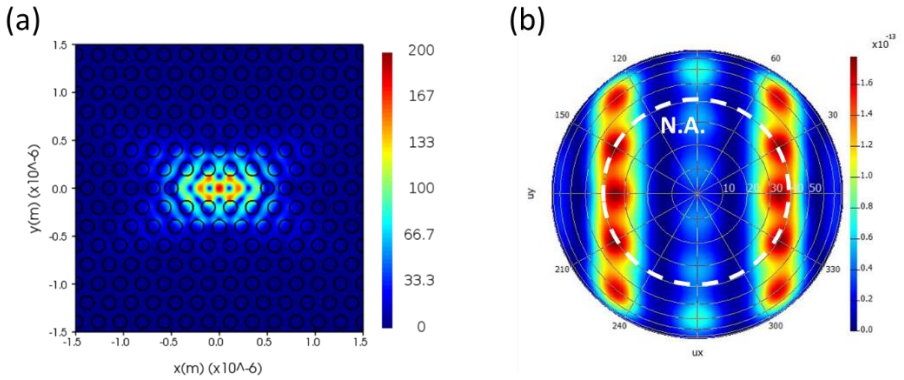

Figure 2.2 Simulation results of L3 cavity with design specified in Figure 2.1(a). (a) Electrical field intensity distribution of the fundamental mode of the L3 Cavity. (b) Far field pattern of the L3 cavity, with numerical aperture (N.A. = 0.65) of the objective lens of the experiment setup (see Appendix A) labelled.

Figure 2.2 is the simulation results of a L3 cavity with the design shown in Figure 2.1 using commercial finite element method (FEM) software (Lumerical FDTD). Figure 2.2(a) is the electrical field intensity distribution of the fundamental mode with its resonance at around 934 nm. As is shown, the majority of the mode is confined in the center of the cavity within in around one micron. The mode volume V is $\sim 0.68\ (\lambda/n)^3$, where n is the refractive index (RI) of GaAs (3.55) and λ is the cavity resonance wavelength. Figure 2.2(b) is the far field projection pattern of the fundamental mode of the L3 cavity. As is shown in (b), most energy can be collected into an objective lens with N.A. = 0.65 used in our setup. However, the far field pattern deviates a lot from standard Gaussian shape, making it inefficient to be coupled into a single mode fiber. Thus a cavity with more Gaussian far field pattern is preferred when high brightness is needed.

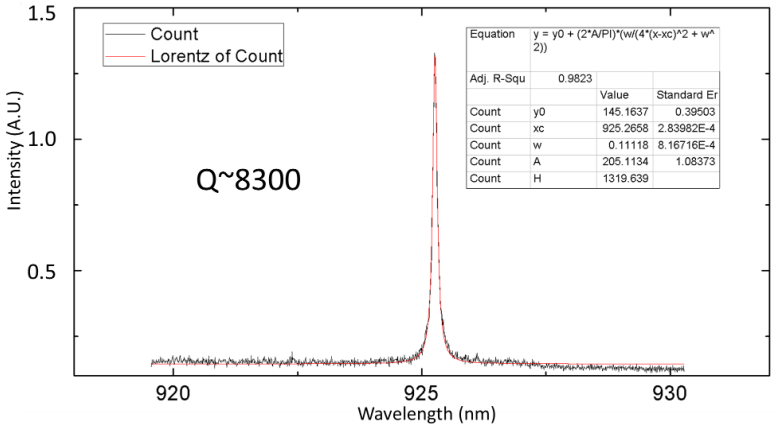

Figure 2.3 Measured PL spectra (black line) of a L3 cavity fabricated using the design in Figure 2.1. Red line is a Lorentz fitting to extract cavity linewidth. The fitted cavity quality factor is around 8300 for this particular L3 cavity.

Figure 2.3 is the measured Photoluminescence of a fabricated L3 cavity on an InAs quantum dots wafer. The linewidth of cavity resonance is around 0.11 nm corresponding to a quality factor around 8300. The measured Q is much smaller than the designed Q, mainly due to the fabrication imperfection and material absorption. The highest Q we have measured on these L3 cavities is around 15,000, and there have been reports of over 50,000 quality factor using pure GaAs slab.[83]

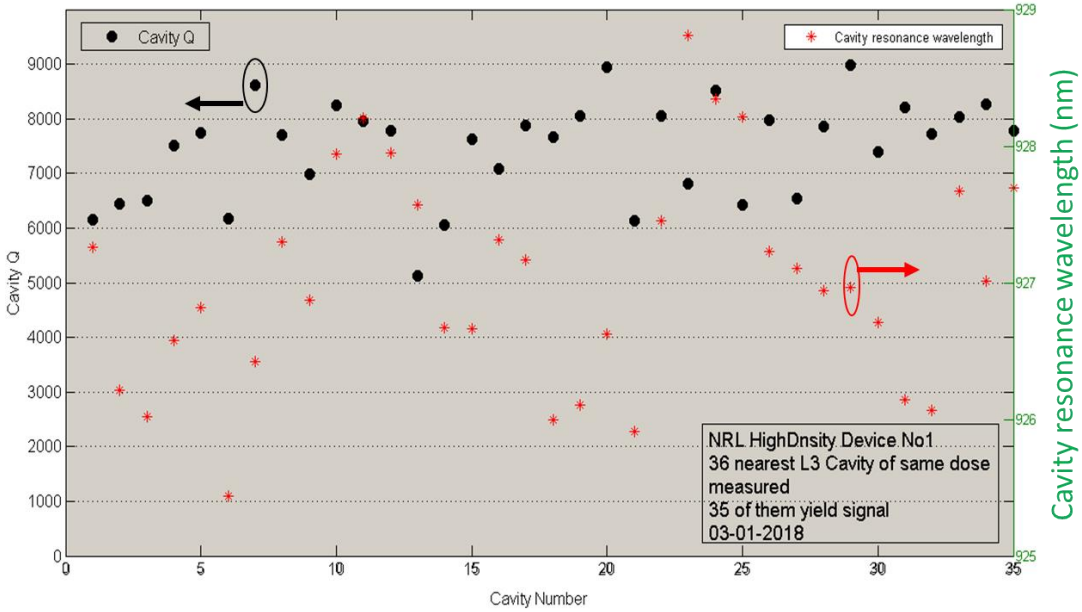

Figure 2.4 Distribution of resonance wavelength and quality factor of L3 cavity fabricated on the same piece of quantum dots wafer. Black points are cavity quality factors. Red data points are cavity resonance wavelengths.

Figure 2.4 is the distribution of resonance wavelengths and quality factors of 35 L3 cavities fabricated on the same chip using the design in Figure 2.1. Their resonances are mainly distributed between 926 nm and 928.5 nm. Most of them have a quality factor between 6000 and 9000. The inhomogeneous distribution of cavity resonance wavelength and quality factor arises from the fabrication imperfections.

The fundamental mode of L3 cavity has very small mode volume and moderate measured Q, which theoretically can give very large coupling strength between its mode and a quantum emitter embedded in it.

2.3 M3 mode of L3 Cavity

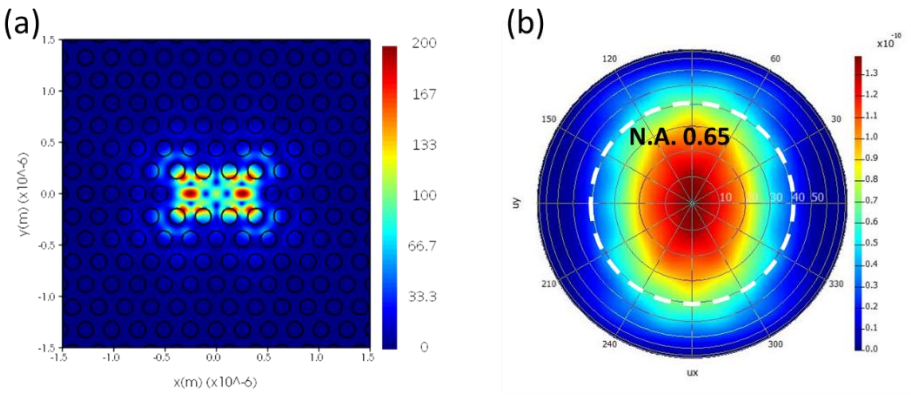

Figure 2.5 FDTD simulation result of M3 mode of L3 cavity. (a) Electrical field intensity of M3 mode with its resonance wavelength shifted to around 930 nm. (b) The far field pattern of M3 mode with N.A. of objective used in lab labeled.

L3 cavity has multiple higher order modes in addition to its fundamental mode. As mentioned above, the fundamental mode of L3 cavity has a non-Gaussian far field pattern, making its coupling into single mode fiber inefficient. The third mode of L3

cavity (M3)[84] instead has a pretty Gaussian far field as shown in Figure 2.5(b). To shift the resonance of M3 mode to match the emission range of InAs quantum dots, the lattice constant of photonic crystal is increased to 255 nm and the radius of air hole is shifted to 77 nm compared to the design of M1 mode in Figure 2.1. The short side of M3 mode is that its quality factor is pretty low, with simulation Q falling at around 1200.

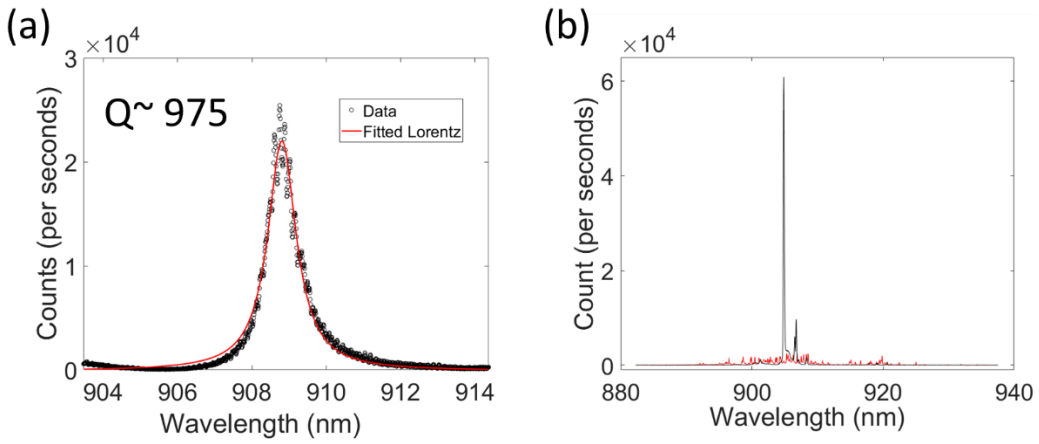

Figure 2.6 Optical measurement of the M3 mode of a L3 cavity with resonance at around 908 nm. (a) Cross-polarized resonant reflectivity spectrum (black circles) of M3 mode excited by a broad band LED with Lorentz fit (Red Line). (b) Photoluminescence of quantum dots inside a L3 cavity (Black Line) and bulk quantum dots (Red Line) excited by an above band laser at around 860 nm.

Figure 2.6 is the optical measurement results of a L3 cavity with its M3 mode shifted to 930 nm band. Figure 2.6(a) is the resonant reflectivity spectrum of M3 mode excited by a broadband Light Emitting Diode (LED) using cross-polarization technique (See appendix A for measurement details). The fitted mode quality factor is around 975 as shown by the red curve in (a), very close to the simulation result. The measured resonance wavelength of the M3 mode (~909 nm) is deviated from its target value of 930 nm because of the fabrication deviations, which can be adjusted through more fabrication trials. Figure 2.6 (b) is the comparison of quantum dots photoluminescence

in (black spectrum) and out (red spectrum) of the cavity region. As is shown in Figure 2.6(b), the brightness of the dots inside the cavity has a gain of more than 30 over the dots in bulk region, which partially justifies the high collection efficiency of the M3 mode.

2.4 Directional Cavity

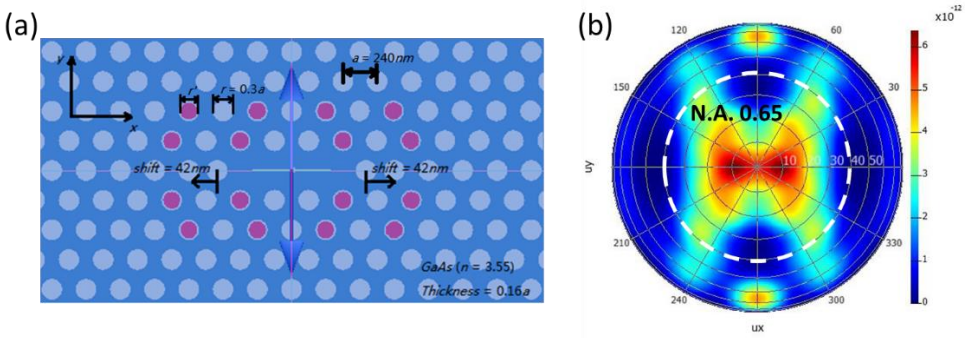

Figure 2.7 Design and simulation of directional cavity. (a) Illustration of design of directional cavity based on L3 cavity. The red holes are the holes whose radius are to be changed to optimize cavity's far field pattern. (b) The far field pattern of a directional cavity with radius of red holes in (a) decreased to 66 nm compare to the normal radius of 70 nm of the remaining holes.

While the M1 mode of L3 cavity suffers from low coupling efficiency into fiber and the M3 mode of L3 cavity suffers from low quality, people proposed a type of new design based on L3 cavity, which is the so-called directional cavity.[79] The design of directional cavity is based on L3 photonic crystal cavity as shown in Figure 2.7. The only difference is that the red holes as indicated in Figure 2.7(a) is enlarged or shrunk compared to normal L3 design. For clarification and simplicity, in the following chapters, we will use Red Hole to refer to the red holes with changed radius in (a). The motivation is to change the propagation vector of cavity's far field emission pattern through the perturbation of the surrounding hole radius to enhance the collection efficiency. While it is a type of perturbation of high Q mode of L3 cavity, its quality factor is supposed to maintain at a high level. Figure 2.7(b) is the simulated far field

pattern of a directional cavity, whose surrounding holes are shrunk to 66 nm compared to the normal radius of 70 nm of the remaining holes. Clearly compared to the M1 mode of L3 cavity, its far field is more Gaussian and most of its far field emission is concentrated within the N.A. of objective lens. The simulation shows that it has a quality factor of around 11,000, very close to the measured Q of a normal L3 cavity.

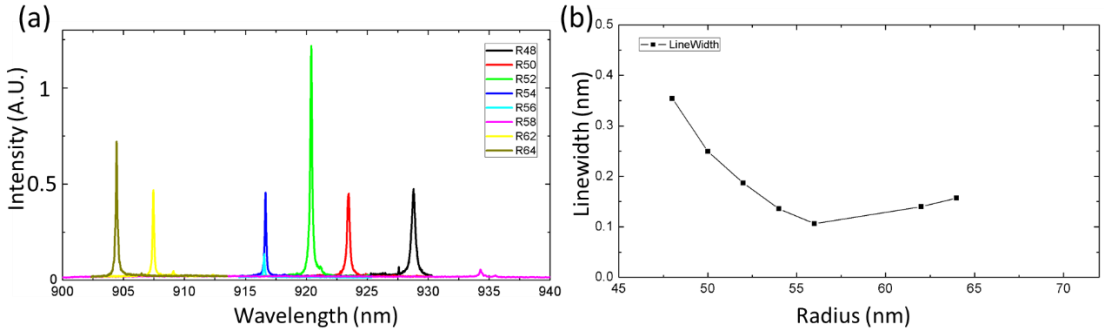

Figure 2.8 Optical measurement results of directional cavities. (a) Photoluminescence spectra of directional cavities with different Red Hole sizes. (b) Linewidth of directional cavities in (a).

When the radius of red holes in Figure 2.7(a) is swept around its normal value (70 nm), there will be trade-off between quality factor and collection efficiency. We fabricated arrays of directional cavities with different Red Hole sizes. Figure 2.8 is the optical measurement results of the directional cavities with varying Red Hole radius fabricated on the same chip. Figure 2.8(a) is the photoluminescence of those directional cavities with Red Hole radius varying from 48 nm to 64 nm as indicated by the legends. The hole radius value in (a) refers to holes drawn in the electronic files (CAD file) used for electron beam lithography (EBL). After the electron beam exposure and dry etching, the real hole size in the end tends to be enlarged compared to the original CAD drawing. In reality, when a 70 nm hole is targeted, 60 nm is used in the CAD file of EBL. As the trend in (a) shows, the resonance wavelength gets shorter as the Red Hole size increases. This is because increasing Red Hole radius would decrease the cavity

length, thus decreases the wavelength of its fundamental mode. Figure 2.8(b) is the linewidth of those cavity resonances in (a). As the Red Hole size is shifted further from its normal value, which brings larger perturbation to the cavity mode, the linewidth increases (cavity quality factor drops).

2.5 H1 Cavity

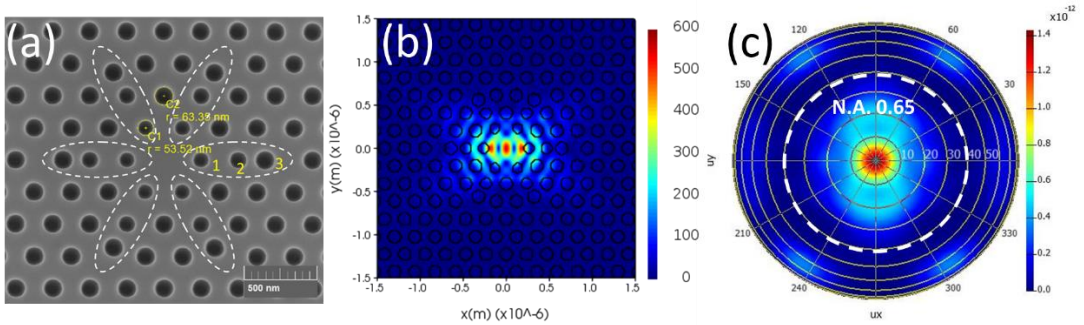

Figure 2.9 Design and simulation result of H1 cavity with the resonance of fundamental mode at around 930 nm. (a) SEM image of a H1 cavity fabricated on InAs quantum dot sample. White circles indicate the position-shifted and size-changed holes of the air hole crystal with a lattice constant a =240 nm. Here, the holes labelled with 1, 2 and 3 are shifted by 0.12a, 0a and -0.26a respectively. The radius of hole 1 and hole 2 are shrunk to 0.24a = 57.6 nm and 0.27a = 64.8 nm respectively. The measured radius of these two holes are 53.5 nm and 63.4 nm as indicated by the yellow circles. (b) Simulated electrical field intensity of x-dipole of the fundamental mode of H1 cavity with design described in (a). (c) Simulated far field pattern of H1 cavity with design specified in (a).

H1 cavity[80] is formed by taking only one air hole away from the photonic crystal. It is principally supposed to be one of the best photonic crystal cavity structures, which simultaneously features small mode volume ($\sim 0.5\ (\lambda/n)^3$), high quality factor (simulation Q > 30,000) and high coupling efficiency into single mode fiber due to its Gaussian far field pattern. It also has two degenerated fundamental modes with orthogonal linear polarizations (x-dipole mode and y-dipole mode), allowing circular polarized light to be coupled into cavity, which is important for spin ration (see Chapter 5). However, the fabrication of H1 cavity is quite challenging, since the positons of the

surrounding holes around the cavity center need to be shifted and their radii need to be shrunk or enlarged. Thus its performance is very sensitive to fabrication errors.

Figure 2.9 is the design and simulation results of the H1 cavity with its resonance wavelength shifted to 930 nm by scaling its lattice constant to 240 nm. The optimization of H1 cavity involves shifting the positions and varying the sizes of the nearest three holes as circled using white dashed lines in Figure 2.9(a) and is a trade-off between its quality factor and far field pattern. With design parameters described in Figure 2.9(a), the simulation gives a quality factor of around 100,000 and a quite Gaussian far field pattern as shown in Figure 2.9(c).

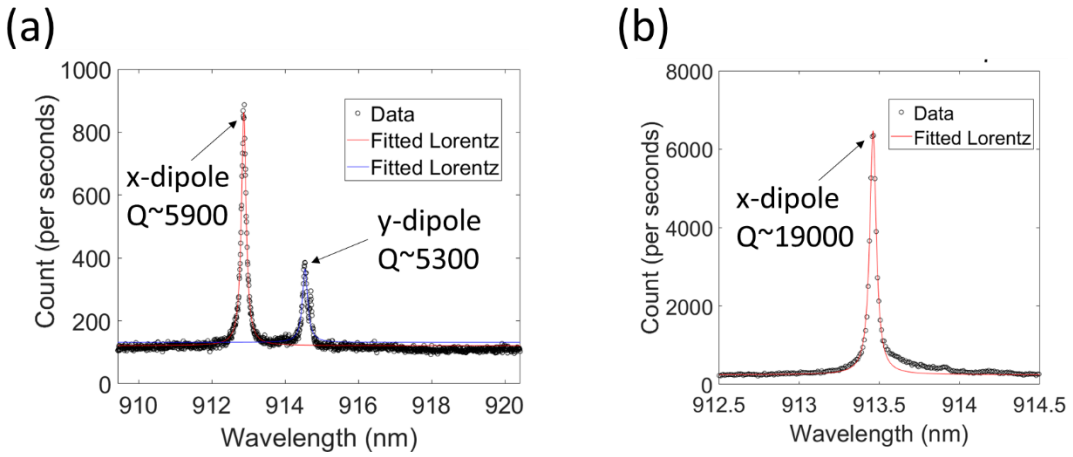

Figure 2.10 Photoluminescence of two H1 cavities fabricated in the same GaAs quantum dots sample with same design parameters. Black circles are the measured data. Solid lines are Lorentz fit.

Figure 2.10 is the measurement results of two H1 cavities fabricated on the same InAs quantum dots sample using the design in Figure 2.9. Figure 2.10(a) is a typical photoluminescence spectrum of H1 cavity. The degeneracy of its x-dipole and y-dipole is lifted due to the fabrication imperfections. The red and blue solid lines are Lorentz fit, which shows that the fabricated Q is around 6000. Figure 2.10(b) is the

spectrum of one of the highest quality factor we have measured on this chip. The y-dipole of this particular H1 cavity is missing, probably due to fabrication errors.

2.6 Bullseye Cavity

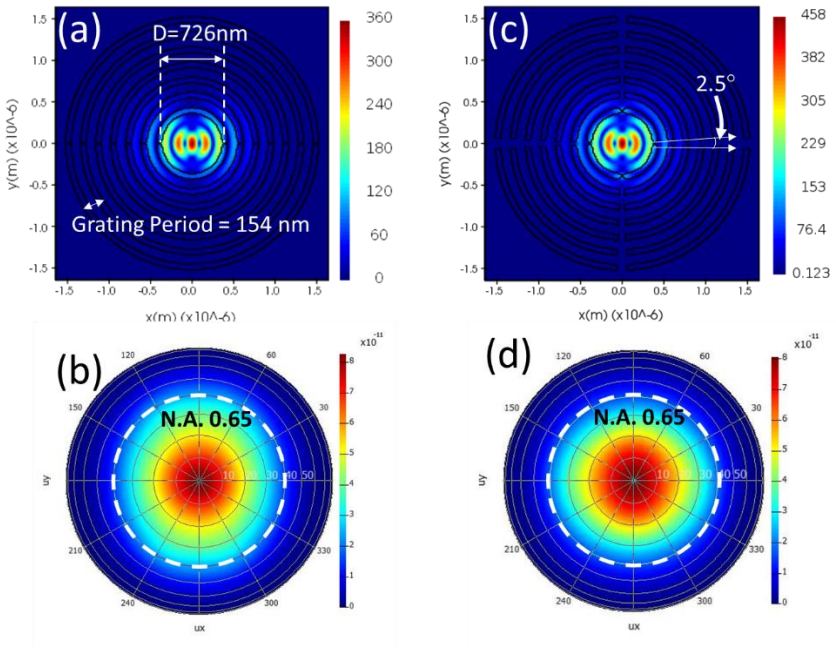

Figure 2.11 FDTD simulation results of the bullseye cavity. (a) Simulated y-dipole mode of Bullseye cavity with resonance at 930 nm. (b) The far field pattern of Bullseye cavity with design shown in (a). (c) The simulated y-dipole field of bullseye cavity with supporting bridges added on top of the design in (a). (d) The far field pattern of (c).

Bullseye cavity[82,85] is a kind of vertical grating coupler that has very Gaussian far field pattern, which is ideal to enhance the collection efficiency from embedded quantum emitters into single mode fiber. So far, people have demonstrated over 50% collection efficiency on single quantum dot using the bullseye structure[20] for the purpose of achieving a bright single photon source. The design and simulation results of bullseye cavities optimized for GaAs slab of 180 nm thickness are shown in Figure 2.11. The bullseye cavity mainly is composed of two parts. One is the center disk that

determines the resonance wavelength of its fundamental mode. For InAs quantum dots eimtting at around 930 nm, we set the radius of the center disk to be 363 nm to target a resonance wavelength of 930 nm. The second part is the surround ring gratings that help shape the Gaussian far field pattern (Figure 2.11(b)), which is related to the radius of center disk and was set to be 154 nm here. To support the grating structure on a suspended GaAs membrane, we added bridges between the gratings to connect them to the bulk region as shown in Figure 2.11(c) and Figure 2.12 below. To minimize the perturbation brought by those extra supporting bridges, we tried to minimize the size of those supporting bridges but made them wide enough to support the weight of the gratings. As shown in Figure 2.11(c), bridges of 2.5° arc with respect to the center of the cavity were used. Figure 2.11 (c) and (d) are the y-dipole electrical field intensity and far field pattern of the bullseye cavity with supporting bridges. Compared to the simulation results of the original bullseye design in (a) and (b), it is clear that introducing bridge structures doesn't affect the optical modes of bullseye cavity much. The simulation shows bullseye cavity typically features a quality factor of around 1000.

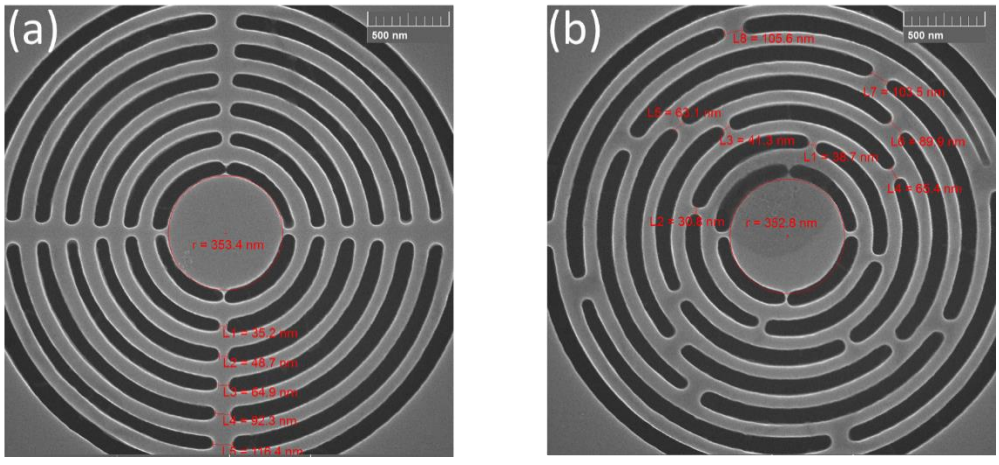

Figure 2.12 SEM images of two bullseye cavities fabricated on the same InAs quantum dots sample.

Figure 2.12 shows the SEM images of two bullseye cavities fabricated on the same chip. The supporting bridges were shifted around in Figure 2.12(b) compared to the original design of (a) for the purpose of reducing perturbation to the cavity field. The radius of the center disk were diminished due to etching and other process of fabrication, causing that the resonance wavelength was blue shifted to around 920 nm compared to the target value of 930 nm (Figure 2.13(a)).

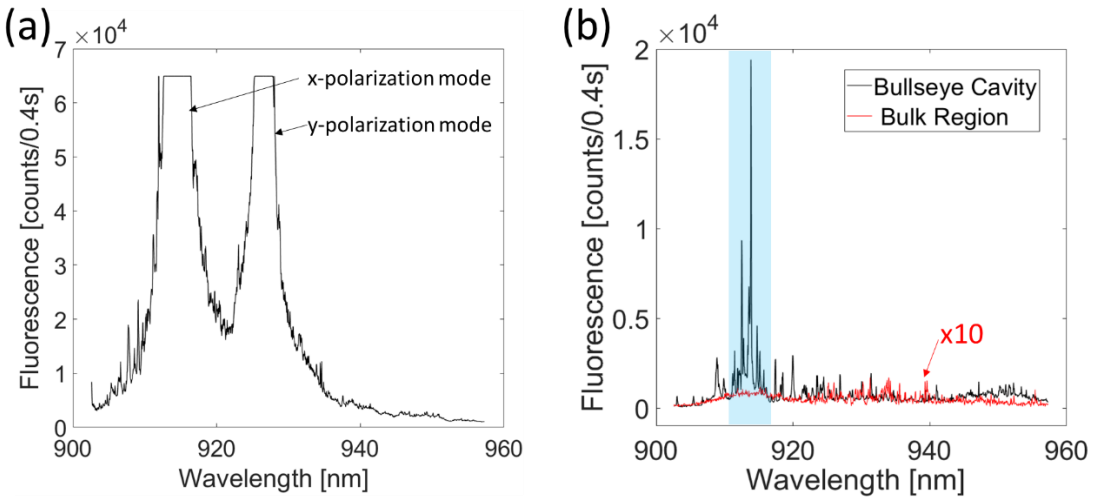

Figure 2.13 Photoluminescence of two bullseye cavities. (a) Bullseye cavity modes excited by above band pumping. The rotation symmetry of bullseye was broken by added bridges and fabrication imperfections. (b) Emission spectrum of quantum dots in (black) and out of (red) the bullseye cavity. The blue shaded region corresponds to the x-dipole mode in (a). The red spectrum is from bulk region and is multiplied by a factor of 10.

Figure 2.13 is the optical measurement results of two bullseye cavities fabricated on the same chip. Figure 2.13(a) shows two orthogonal resonance modes of the bullseye cavity illuminated by the quantum dots inside the cavity. The original degeneracy of its fundamental modes of different polarizations due to its rotational symmetry is broken by the added supporting bridges and the fabrication imperfections. Under similar measurement conditions used in characterization of above-mentioned photonic cavities, the photoluminescence of those bullseye cavities easily saturated the

CCD camera as shown in Figure 2.13(a), which indicates that they have pretty good coupling efficiency into the single mode fiber.

Figure 2.13(b) is the photoluminescence of another bullseye cavity containing several bright quantum dots emission peaks. The bright dots region which is labelled by the blue shadow is very close to the wavelength of the x-polarization mode of the bullseye cavity in (a), which is a strong indication that their high brightness compared to the dots in bulk region (red spectrum in (b)) is a result of the collection enhancement brought by bullseye cavity.

2.7 Conclusion

In this chapter, five common types of optical cavities are explored. For the purpose of a strong spin-photon interface, several goals or criteria need to be considered during the selection and optimization of photonic cavities: (1) High quality factor Q and small mode volume V to achieve strong light-matter interaction, since the coupling strength between the emitter and cavity mode g, is proportional to $g \sim Q/\sqrt{V}$. (2) High collection efficiency into single mode fiber, which means Gaussian far field pattern. (3) Degenerated modes with orthogonal polarizations which allows efficient electron spin rotation using laser field (see Chapter 5 for details of spin rotation using laser). The goal of (1) and (2) can sometimes contradict to each other because better coupling efficiency usually means larger cavity coupling loss. Since total cavity quality factor Q is inverse of cavity loss κ, and can be written as $Q_{total} = Q_{internal} + Q_{couping}, Q_{internal} = 1/\kappa_{internal}$, $Q_{coupling} = 1/\kappa_{coupling}$, thus larger coupling efficiency will decrease the cavity quality factor.

Table 1 Summary of Photonic Cavities Design

	Design Q	Measured Q (Waks)	Mode Volume	Collection Efficiency	Mode Polarization
M1 mode, L3 Cavity	>120,000	8000-30,000	$0.68(\lambda/n)^3$	Low	one linear polarization
M3 mode, L3Cavity	~1200	~1000	$0.77(\lambda/n)^3$	high	one linear polarization
Directional Cavity	5000-30,000	2000-10,000	$0.81(\lambda/n)^3$	medium	one linear polarization
H1 Cavity	~95,000	5000-19,000	$0.53(\lambda/n)^3$	high	two linear, orthogonal
Bullseye Cavity	~1200	~500	$1.3(\lambda/n)^3$	best	support all polarization

Table I is a performance summary of above discussed cavities in this chapter. It is clear that H1 is the best candidate that satisfies all the requirements for strong spin-photon interface. When cavity QED effects are not required, bullseye cavity would be the best choice since it is easy to be fabricated. It is also worth mentioning that the fabrication imperfections would lift the mode degeneracy of H1 and bullseye cavities as shown by the measurement results. A lot of methods have been proposed to overcome this problem[86,87]. Also among all those cavities, H1 cavity requires the most significant tuning of its surrounding holes' positions and sizes. Its performance (quality factor and far field pattern) is also very sensitive to the variation of those tuning parameters. Therefore H1 turns out to be the most challenging one to fabricate. The small cavity spatial size also makes H1 cavity have the lowest yielding in terms of finding a QD inside the cavity area, since QDs are random distributed over the wafer and smaller cavity volume means lower probability to find a quantum dot inside the cavity. Due to these two reasons, H1 cavity was not used in the following chapters of

this thesis research. Instead, when we tried to explore the strong coupling between QDs and photonic cavities, L3 cavity was used since it could stably produce measured quality factor above 8000 and has a relatively larger cavity size. To study the spin properties, bullseye cavity was used because the spin readout and control experiments requires stronger optical signal.

Chapter 3: Spin-dependent Resonant Cavity Reflectivity

3.1 Chapter Introduction

Photons have limited direct interaction with each other. One way to mediate their interactions is using a cavity QED system, where the cavity reflectivity is strongly dependent on atom state. In such system, the early incident photons can change the cavity resonant reflection coefficient by changing the atom's state, thus modulating the later incident photons. Such scheme has been proposed to achieve many important applications for quantum network, like building a quantum phase gate and generating multi-dimensional photon entanglement. In this chapter, I will present such cavity QED system based on a charge tunable InAs quantum dot strongly coupled to a L3 cavity.

3.2 Device Characterization

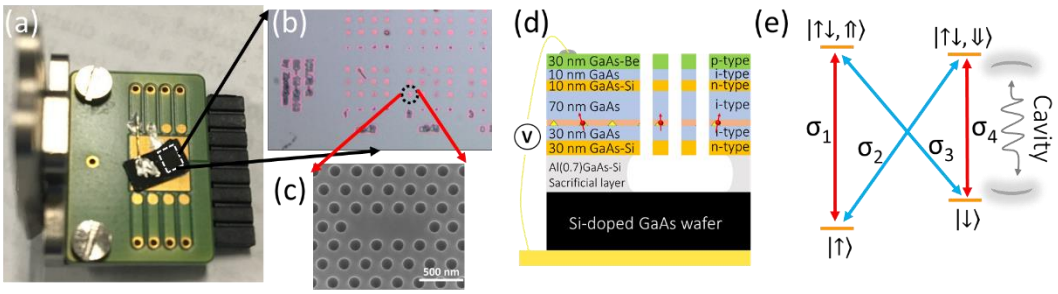

Figure 3.1 Device Structure. (a) Picture of wired device on a chip carrier. (b) Optical microscope image of fabricated L3 cavity matrix on a GaAs quantum sample piece. (c) SEM image of one of the L3 cavity in (b). (d) The layered structure of wafer used in (a) showing a p-i-n-i-n diode with a 30 nm electron tunneling barrier. (d) The energy-level diagram of a single electron-charged quantum dot coupled to a microcavity under a magnetic field in the Voigt configuration. Only transition σ4 is on-resonance with the cavity.

Figure 3.1 shows the device structure used in this chapter. (a) is the picture of the wired device in a chip carrier. As shown in (d), the top and bottom of the sample were wired to two pins of chip carrier using conductive epoxy cure in 120 degree for

30 minutes. (b) is the optical microscopic image of the L3 cavity arrays pattered on chip using EBL. Matrix of exactly same L3 cavities were patterned over the chip surface. Around 500 cavities were characterized before around 20 of them were found to have a quantum dot within 2 nm of the cavity resonance wavelength showing signature of strong coupling. The following experiments were performed based on one of such cavity with label 3113.

In order to trap and stabilize an electron in the quantum dot to form this four-level system, we utilize a device structure featuring InAs quantum dots embedded in a p-i-n-i-i-n GaAs diode membrane of 180 nm in thickness (layered structure shown in Figure 3.1(d)). In this membrane we patterned L3 photonic crystal cavities[88] (scanning electron microscopy image shown in Figure 3.1(c)) that featured a high-quality factor ($\sim 10^4$). We used an optical cryogenic setup similar to that in Sun *et al*.[34] to measure the photoluminescence and cross-polarized reflectivity spectrum of the quantum dots and cavity. Details about the device fabrication and optical measurements can be found in the Appendix A and B.

Figure 3.1(e) is the energy-level diagram of a negatively charged quantum dot under an external in-plane magnetic field (Voigt geometry). It features two opposite electron spins (spin up and spin down) that form the two ground states, labelled as $|\uparrow\rangle$ and $|\downarrow\rangle$, respectively. Meanwhile an electron pair with the opposite hole spin form the two excited states, labelled as $|\uparrow\downarrow, \Uparrow\rangle$ and $|\uparrow\downarrow, \Downarrow\rangle$.[55] An in-plane magnetic field can be applied to break the energy degeneracy of the opposite spin states, enabling us to

individually address the four optically allowed and linearly polarized transitions (σ_1 to σ_4).

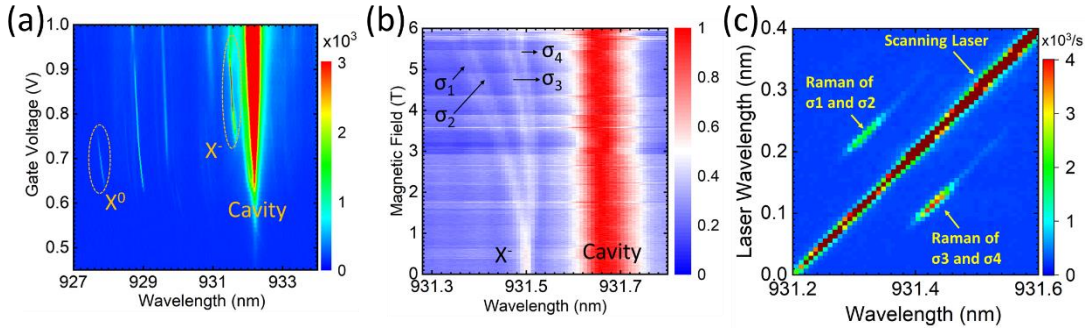

Figure 3.2 A single electron charged quantum dot near the cavity resonance. (a) Photoluminescence spectra of quantum dots and the cavity at different gate voltages. Inside the dashed circles are the neutral exciton state (X^0) and single electron charged state (X^-) of a quantum dot. (b) Cross-polarized reflectivity spectrum under different magnetic fields (0–6 T, Voigt configuration). The single emission peak of the quantum dot splits into four emission peaks with increasing magnetic field amplitude, corresponding to the four optical transitions (σ1 to σ4, from short to long wavelength) shown in (c). (c) Raman emissions from the four-level charged quantum dot when scanning the pumping laser wavelength across the four optical transitions at 6.2 T and 0.87 V.

Photoluminescence spectrum of the cavity at different gate voltages were measured to identify the charging states of the embedded quantum dots. Figure 3.2(a) shows the measured spectra as a function of the voltage bias. A quantum dot with a resonance frequency of ~927.7 nm (labelled X^0) emits at a bias voltage range of 0.64–0.74 V, while at a higher voltage range of 0.73–0.99 V we observed another emission at ~931.5 nm (labelled X^-). These states correspond to a neutral and charged exciton emission. The bright peak near 932 nm (labelled "Cavity") is the L3 cavity mode illuminated by nearby quantum dot emissions. The X^- peak is much brighter than the X^0 peak due to Purcell enhancement by the nearby cavity mode.

To determine the charging state of X^- in Figure 3.2(a), we measured its reflectivity spectrum under increasing external magnetic field (Voigt-geometry) using

cross-polarized resonance reflectivity spectroscopy (Figure 3.2(b)). For these measurements, the gate voltage was set to 0.87 V to stabilize the X^- state, where it features the strongest signal and narrowest linewidth (Figure 3.2(a)), indicating the diode bias was set at the maximized spin lifetime for this particular dot. The single X^- peak at low magnetic field splits into four peaks at high field (> ~3T), indicating a four-energy level system, which suggests a charged quantum dot state (i.e., a trion; Figure 3.2(b)).

To confirm the energy levels shown in Figure 3.1(e), we scanned the wavelength of a narrow linewidth laser through the four optical transitions at 6.2 T (Figure 3.2(c)). The strong diagonal signal in Figure 3.2(c) arises from direct reflection of the scanning laser off of the sample surface. When the laser wavelength is close to σ1 and σ2, it produces Stokes emission close to σ3 and σ4 in wavelength, while exciting near the σ3 and σ4 transitions produces Anti-Stokes emission close to σ1 and σ2. The wavelength difference between the scanning laser and the Raman emission it produces corresponds to the splitting between the two ground states of the quantum dot, which we determined to be 0.12 nm at 6.2 T (Figure 3.2(b)). From the peak wavelength of the Raman signal, we estimated that σ1 and σ2 are near 931.32 nm while σ3 and σ4 are near 931.44 nm, which is in agreement with the wavelength of these four transitions shown in Figure 3.2(b). The observation of Raman emission induced by the pumping laser also confirms we can use the spin-flip process accompanying the Raman emission to initialize the spin state, which is also called optical pumping.

In order to determine whether the X- state is due to a hole or electron charging event, we calculated the Lande g-factor of this quantum dot using the equation $g_l = \hbar\Delta_e/\mu_B B$, in which Δ_e is the energy splitting between two trion ground states under an external magnetic strength of B, μ_B is the Bohr magneton. For this system, we found a Lande g-factor of $g_l \approx 0.47$, which is consistent with the 0.4–0.6 range reported for a single-electron-charged quantum dot.[34,72,89–91] Furthermore, the X^0 and X^- states are separated by ~3.8 nm (Figure 3.2(a)), which is consistent with the previously reported trion binding energy of an InGaAs quantum dot.[36,92–94] This combined evidence suggests that X^0 and X^- are the neutral and negatively charged states of the quantum dot, respectively.

3.3 Tuning of Cavity Wavelength using IPA

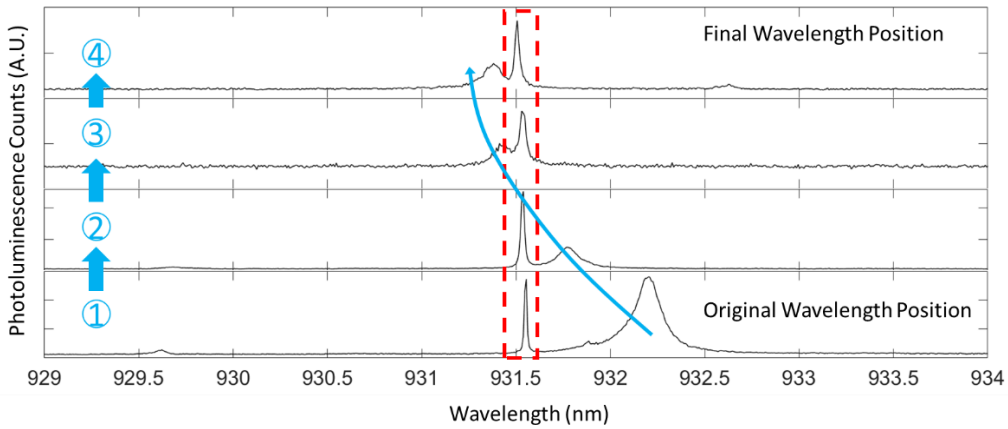

Figure 3.3 Photoluminescence Spectra of cavity 3113 after being cleaned by IPA. The Red dash box showing the position of the dot emission line. The blue curved arrow shows the trace of the shift of cavity resonance wavelength. Note the emission wavelength of QD was almost stayed unchanged. Only the cavity resonance shifted a lot due to change of effective refractive index.

To enable the charged quantum dot to modulate the cavity reflectivity under an external magnetic field, it was necessary to bring one of the trion transitions on-resonance with the cavity. However, trion transitions shift toward shorter wavelengths

with increasing magnetic field due to diamagnetic effect, as shown in Figure 3.2(b). Therefore we shifted the cavity wavelength to the shorter side of the quantum dot emission at 0 T (~931.45 nm, Figure 3.3) by performing a surface cleaning treatment. We then applied a magnetic field to break the trion energy degeneracy and shift one of the transitions on-resonance with the cavity *via* the Zeeman Effect to achieve coupling.

3.4 Characterization of Strong Coupling

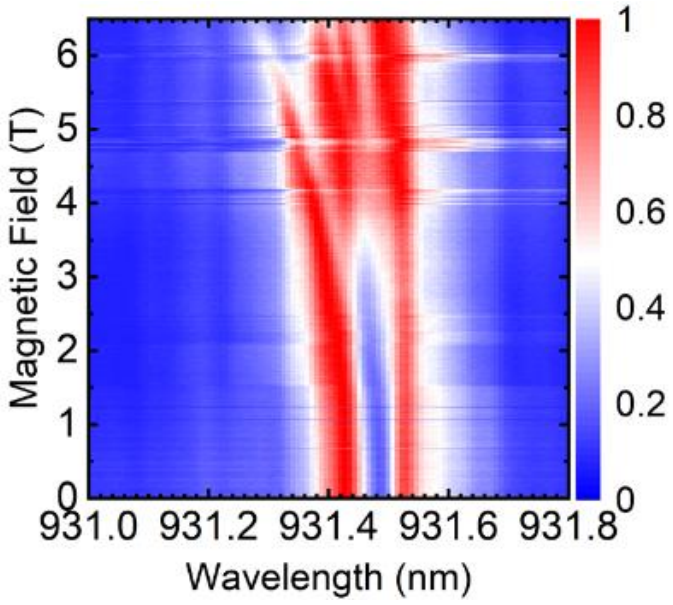

Figure 3.4 Normalized reflectivity spectra versus the Voigt-geometry magnetic field amplitude from 0 to 6.5 T at 0.87 V. The spectral jumps and wandering observed here are also due to sample stage realignment in response to the magnetic field as in Figure 3.2(b).

Figure 3.4 is the reflectivity spectra as a function of this magnetic field amplitude at 0.87 V, excited by a broadband light emitting diode. In contrast to Figure 3.2(b), where the cavity and dot are clearly separated in emission wavelength, the emission spectrum in Figure 3.4 exhibits multiple anti-crossings between the different trion transitions (σ_1–σ_4) as they are tuned across the wavelength of the cavity mode

due to the strong coupling between the quantum dot and the cavity.[41,95,96] At ~6 T, transition σ_4 is near on-resonance with the cavity. We note that σ_3 is also coupled to the cavity with a slight detuning under these conditions due to the small splitting between the two excited states (~0.04 nm at 6 T).

3.5 *Spin-dependent Cavity Reflectivity*

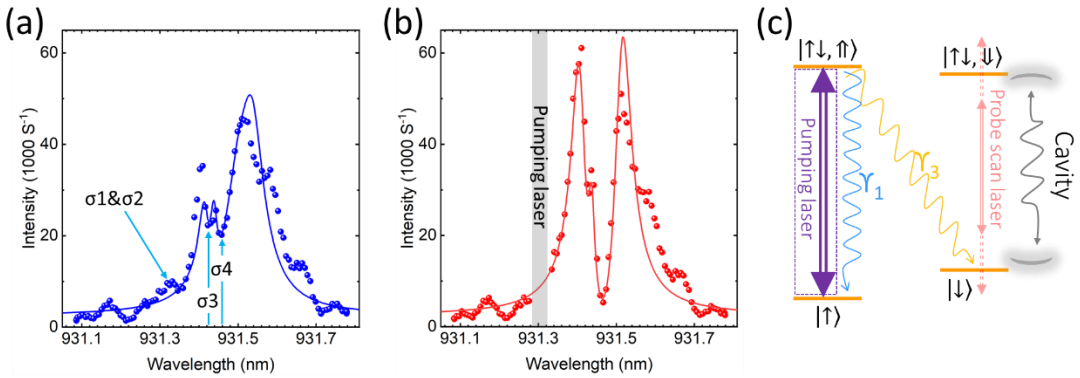

Figure 3.5 The effect of optical pumping on the spin population and cavity reflectivity at 0.87 V and 6.2 T. (a) The cross-polarized reflectivity spectrum (blue dots) measured without laser pumping. The blue solid line is the numerical fitting. The blue arrows indicate the wavelength positions of the quantum dot's four optical transitions. (b) The cross-polarized reflectivity spectrum (red dots) measured with the pumping laser on resonance with transition σ1. The data points near 931.32 nm were discarded because of the strong reflected signal from the optical pumping laser at that wavelength. The red solid line is the numerical fitting using the same model as (a). (c) Schematic diagram of the experiment in (b). A pumping laser resonant with transition σ1 was used to initialize the electron population to the |↓⟩ state. Υ_1 and Υ_3 are the spontaneous emission induced by the pumping laser, which have the same wavelength as transition σ1 and σ3, respectively. Υ_3 is the spin-flip process that brings the spin population from |↑⟩ to |↓⟩. A weak tunable laser was scanned across all the transitions to probe the cavity reflectivity spectrum.

We therefore fixed the magnetic field at 6.2 T where σ_4 is near on-resonance with the cavity to study how the quantum dot spin state affects the cavity reflectivity. We first measured the cavity reflectivity at thermal equilibrium (Figure 3.5(a)) by scanning a tunable narrow linewidth laser, which was weak enough to avoid optically pumping the electron spin. The observed two dips in the spectrum at 931.42 nm and 931.46 nm correspond to transitions σ3 and σ4, respectively. These dips are due to the

cavity reflectivity modification brought by the destructive interference between the quantum dot transitions and cavity field. The relative depth of those dips depends on the atomic cooperativity between the transition and the cavity, defined as $C = 2g^2/\kappa\gamma$, where g is the coupling strength between the individual transition and cavity, and κ and γ are the decay rate of the cavity and the quantum dot transition. We measured $\kappa/2\pi = 31.79\ GHz$, corresponding to a quality factor around 10,000. Transitions σ1 and σ2 near 931.32 nm are too weak to be resolved in this spectrum because of large detuning from the cavity.

The depths of the two dips in the reflectivity spectrum are poor because the spin state of the quantum dot is not in the pure $|\downarrow\rangle$ state but rather a mixed state of $|\uparrow\rangle$ and $|\downarrow\rangle$, with a probability of P_{up} and $P_{down} = 1 - P_{up}$, respectively, determined by thermal equilibrium. Accordingly, the reflectivity spectrum of the mixed state (R_m) can be viewed as a probabilistic superposition of two individual spectra, R_{up} and R_{down}, quantified as $R_m = P_{up}\, R_{up} + (1 - P_{up})\, R_{down}$,[34] where R_{up} and R_{down} are the reflectivity spectra when the quantum dot spin is in the pure $|\uparrow\rangle$ or $|\downarrow\rangle$ state, respectively. R_{up} can be approximated by the bare cavity reflectivity (i.e., without any quantum dot emission; Figure 7.3(b)), since when the spin population is in the $|\uparrow\rangle$ state, the quantum dot can only make transitions σ1 and σ2 (Figure 3.1(e)), which are largely detuned and thus not coupled to the cavity. When the population is in the $|\downarrow\rangle$ state, the quantum dot can only make optical transitions σ3 and σ4. Thus the reflectance at the cavity resonance wavelength will be strongly suppressed and appear as a dip in the spectrum due to the destructive interference between σ4 and the cavity field. We fit the

reflectivity results in Figure 3.5(a) to a theoretical model (blue line) and extracted P_{up} to be 0.52. While theoretically, the population occupation at thermal equilibrium should be proportional to $e^{-\Delta E/k_B T}$, from which we calculated P_{up} to be 0.39, with $\Delta E \sim 0.165\ meV$ (energy splitting between $|\uparrow\rangle$ and $|\downarrow\rangle$, 0.12 nm) and $k_B T \sim 0.362\ meV$ (at 4.2 K). We attribute the deviation of the experimentally extracted value of P_{up} from the theoretical prediction to the distortion of reflectivity spectrum caused by the inevitable etaloning fringes of the optical setup.

We used optical pumping[34,90,97] to move the system out of thermal equilibrium and initialize the quantum dot to the spin-down state to observe the resulting change in the cavity reflectivity. We chose to resonantly drive transition σ1 using an optimal pumping wavelength and power (931.32 nm, 120 μW) because driving σ2 would introduce Raman emission near the cavity resonance wavelength, which would interfere with the reflectivity measurements. As we pumped this transition, we simultaneously probed the system's cavity reflectivity (Figure 3.5(b)). The dip at 931.47 nm created by the interference between the cavity and the quantum dot emission field is more significant compared to that in Figure 3.5(a) because the optical pumping initializes more spin population to the $|\downarrow\rangle$ state. Figure3.5(c) demonstrates the schematic diagram of this pump and probe experiment.

We fit the spectrum (red line Figure 3.5(b)) and extracted $P_{up} < 0.02$ (95% confidential bound), which shows we were able to initialize most of the spin population to the $|\downarrow\rangle$ state, consistent with a previous report[90]. Based on this fitting, we also extracted the detuning between the σ4 transition and cavity to be within $2.8\ GHz$,

confirming that σ4 was near resonance with the cavity. The corresponding coupling was $g_4/2\pi = 17.2 \pm 0.6$GHz. The coupling between the σ3 transition and cavity was thus $g_3/2\pi = \sqrt{g^2 - g_4^2} = 7.2$ GHz. We believe the difference between σ3 and σ4's coupling strength with the cavity is due to the different polarization alignment of σ3 and σ4 with the cavity field polarization. From the fitting, we also extracted the dephasing of σ4 and σ3 to be $\gamma_{d4}/2\pi = 1.4 \pm 0.4\ GHz$ and $\gamma_{d3}/2\pi = 3.1 \pm 1.5 GHz$, respectively. From these derived parameters, we calculated the cooperativity between σ4 and the cavity to be $C = 2g^2/\kappa\gamma = 12.4$, which is a significant improvement from previous reports of coupled negatively charged quantum dot-cavity systems (C~2).[34,37,94] We attribute this improvement partially to the increased charging stability imposed by the diode. The system also satisfies the strong coupling criteria ($4g > \kappa + \gamma$), meaning it operates in the strong coupling regime[95,96,98]. We also tried optically pumping σ3 to transfer the population to the spin-up state. However, because the detuning between σ3 and σ4 is small (12 GHz (0.04 nm) separation), we cannot resolve the probe laser from the direct reflection of the stronger optical pumping laser.

3.6 Conclusion

In conclusion, we have achieved spin-dependent cavity reflectivity within a charge tunable device. The diode structure allows us to deterministically load and stabilize electron spin inside quantum dots, which leads to a cooperativity as high as 12. Using samples with a bottom distributed Bragg reflector could increase the device signal collected. Additionally, integrating the cavity with a tapered fiber[99] or on-chip waveguide[100] would allow higher signal collection efficiency. Increasing the quality

factor of the L3 cavity to over 50,000[101] could also lead to a much larger atomic cooperativity. The strong solid state spin and photon interface demonstrated in this work could enable many quantum information processing tasks, such as deterministic spin-photon entanglement[102] and single-shot spin readout,[103] and could be used as a building block for future quantum networks linked by photonic qubits.

Chapter 4: Quantum dot spin T1

4.1 Chapter Introduction

The storage and processing of quantum information requires that a qubit has a long coherence time (T2) and lifetime (T1), where T2 is limited by T1 through $2 * T2 < T1$.[49] Unlike real atoms such as cold atoms and trapped ions which are quite isolated from environment, solid state spin systems are usually strongly coupled to their host reservoir. Thus their spin properties can be affected by many factors like phonons,[50] nuclei spins,[64,104] charge fluctuations.[60] Those couplings to the solid state environment tend to degenerate their spin properties and make them strongly sample dependent. Even within the same wafer, the local micro-environment can be quite different, leading to inhomogeneous distribution of various properties of those spins. Compared to other solid state system like defects in diamond and rare earth ions, self-assembled QDs are more prone to be affected by solid state environment, since more atoms (~10^5) are involved in a single quantum dot.[104]

Electron spin confined in self-assembled InAs quantum dots has been reported with T1 lifetime up to millisecond.[12,15,56,66] But most of the published work so far show a T1 lifetime in the microsecond regime of those dots.[69,71,93,103] The mechanism of the spin flip process in GaInAs dots has been well studied, where the phonon assisted spin-flip process is the major spin decay channel and the flip rate is scaled to B^5 as the magnetic field increases, where B is the magnetic field strength. While reducing external magnetic field would certainly increase QDs T1, magnetic field in the Tesla regime is necessary to create observable energy gap between two spin ground states,

making four optical transitions of QDs being individually addressable. For those dots sandwiched in PN diode, electron tunneling between the dot and the electron Fermi sea can sometimes be the T1 limiting factor.[64,105] Recent study has shown that when the magnetic field is small and thus Phonon induced flip is slow, the T1 is dominated by electron tunneling process.[56] During our experiments, we realized that the T1s of all our samples were very short (as short as several tens of nanoseconds) and finally limited their coherence time. In this chapter, we measured T1 across multiple samples with different wafer vertical layer structures and we show that T1 of QDs spin can be destroyed by off-resonant laser applied to rotate the spin.

4.2 Measurement Technique

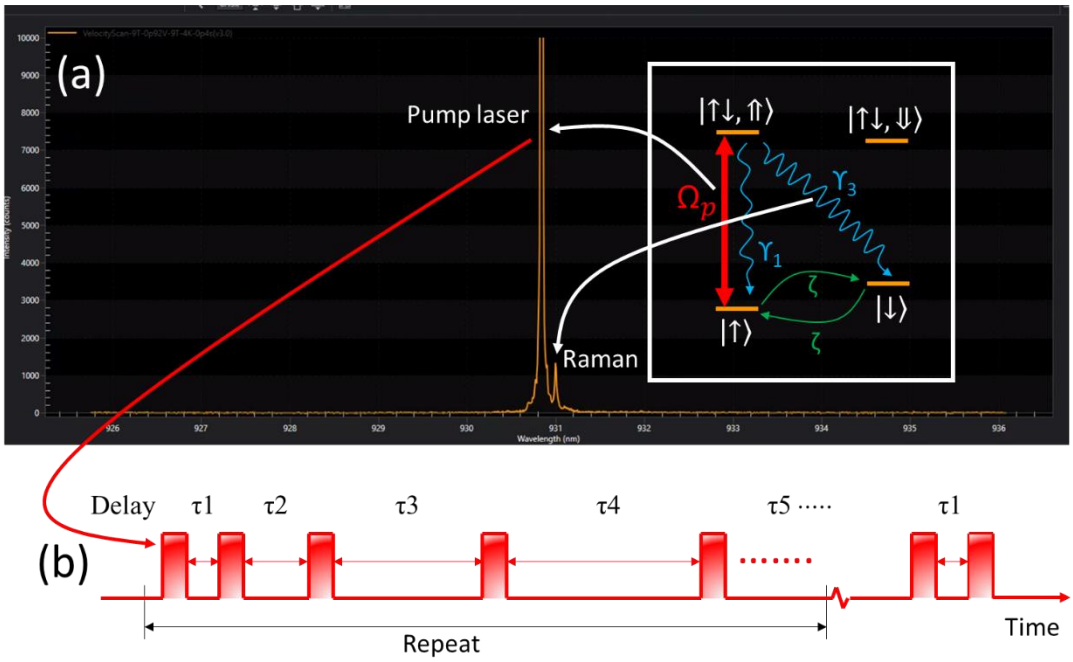

Figure 4.1(a) Spectrum of T1 experiment of InAs quantum dot spin. A laser resonant with transition σ1 is driving the four level system with Rabi frequency Ω_p as the insert shows. The excited state has two spontaneous emission channels leading to the two ground states with decay rate Υ_1 and Υ_3 respectively. The spin has a relaxation rate ζ between its two ground states $|\uparrow\rangle$ and $|\downarrow\rangle$. (b) Illustration of the resonant laser pulse used to measure T1 lifetime of QD electron spin. The optical pulse train was produced by modulating a CW laser going through a fiber-based electro-optic modulator using RF signal generated by an arbitrary waveform generator (AWG).

We used a common pump-delay-probe way to measure the spin lifetime.[15,69] Figure 4.1(a) is the spectrum of a typical T1 measurement. A pulsed laser resonant with one of the four optical transitions of QD is used to initialize the spin to one of the ground state as the insert shows. When the QD is brought to its excited state, it can spontaneous decay to two ground states. If the QD returns back to its original ground state, then it will be pumped by the driving laser again until all the population is initialized to the other ground state. Over 99% spin initialization fidelity have been reported with CW laser or laser pulse of several nanoseconds long[69,90]. After some time delay, the spin will relax back to its original state due to various spin relaxation mechanism as mentioned above. At this point, we can apply the same pumping laser pulse again, the resulting Raman count will be proportional to the population relaxed back to the original spin state. By varying the delay between first and second pump laser pulse and monitoring the resulting Raman counts, we can extract the spin relaxation time. Figure 4.1(b) is the scheme of the laser pulse used to read out the T1. Multiple laser pulses with different time delays between them are produced by modulating a CW laser using a 30 GHz electro-optic modulator. The pulse shape was printed into optical pulse from the Radio Frequency (RF) signal out of an arbitrary waveform generator (AWG). Each laser pulse serves both as a pump laser to initialize the spin state and also as a probe laser to read out the spin population. The laser pulse usually has a duration of several nanoseconds to ensure the complete initialization of the spin state. The Raman signal shown in Figure 4.1(a) caused by the laser pulse train will be filtered out by a spectrometer and then sent to a SPCM so we can get the time-resolved Raman counts corresponding to each pump laser pulse.

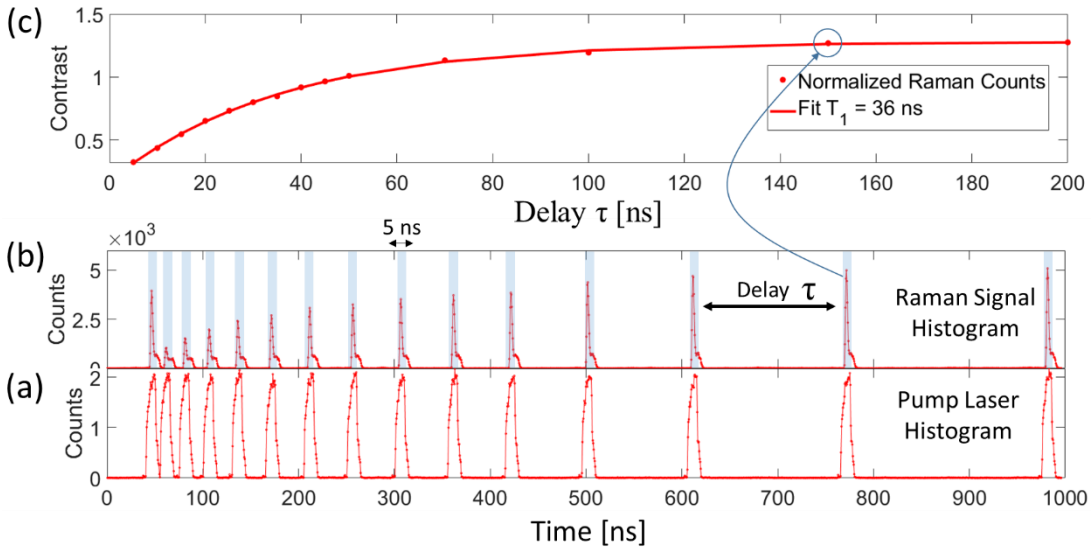

Figure 4.2 Illustration of T1 measurement data from Sample R111101F. (a) Pump laser pulse train measured on a SPCM. (b) The resulted Raman signal corresponds to the pump laser in (a). (c) The added counts of initial 5 nanoseconds (blue shadow in (b)) of each Raman pulse versus the time delay between adjacent pump laser pulses. The exponential fitting shows this dot has a T1 lifetime of 36 nanoseconds.

Figure 4.2 illustrates a typical dataset of T1 measurement. Figure 4.2(a) is the pump laser pulse train measured on a SPCM after being filtered out by the spectrometer. The on-off extinction ratio of the laser pulse can reach around 30 dB, which is primarily limited by the extinction ratio of EOM we have. Figure 4.2(b) is the resulted Raman signal pumped by the laser pulse train in (a) measured on SPCM. The spike at the beginning of each Raman signal pulse (blue shadow area) is due to the spin population that relaxes back to original spin state during the time interval between two consecutive pump laser pulses. Each Raman pulse has a non-zero floor count due to the short T1 lifetime (large relaxation rate). Figure 4.2(c) plots the normalized Raman count spike of each Raman pulse in (b) versus its delay with respect to the Raman pulse to its left. Each data point in (c) is normalized to the added count of the first Raman

pulse spike in (b). The data is fitted to exponential, $B + A * e^{-T1/\tau}$, to extract the T1 lifetime. B and A are the background and scaling factor used as free fitting parameters.

4.3 T1 of Different QD samples

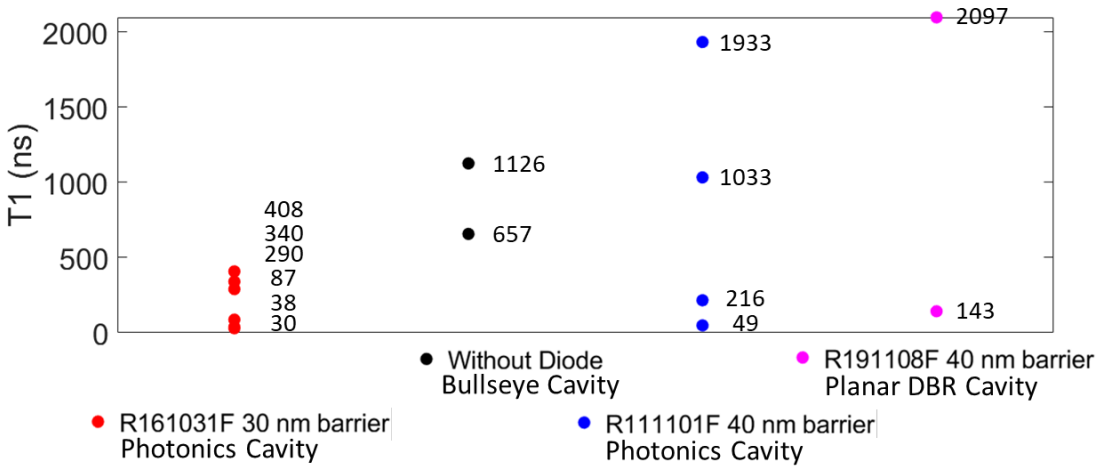

Figure 4.3 QDs electron spin T1 measured on different samples at 6 Tesla. Red data points were measured on QDs in L3 photonic cavity fabricated on wafer R161031F with 30 nm tunneling barrier. Black data points were from dots inside bullseye cavities fabricated on QDs wafer without diode structure. Blue data points were measured on QDs in L3 photonic cavity fabricated on wafer R111101F with 40 nm tunneling barrier. Magenta data points were from bulk dots inside a planar DBR cavity with 40 nm tunneling barrier.

By the time of writing this dissertation, we have measured spin properties of two major types of InAs quantum dots we have. One is QDs buried in various PN diode structure (charge-tunable dots) with basic layered structure shown in Figure 1.1(b). The other is those tradition QDs without diode structure similar to the one shown in Figure 1.1(a). For the charge tunable dots, the key difference among them are the tunneling barrier thickness between the QDs layer and the n-type doped layer beneath them (See Figure 1.1(b)). So far, we have two different tunneling barrier thicknesses, most of the wafers have a 30 nm barrier and several of them have a 40 nm barrier. In the QDs community, we have seen reports of tunneling barrier varying from 20 nm to 60

nm.[56,69,93] Some of the wafers have extra AlGaAs blocking layer with thickness up to hundred nanometers to further reduce the electron tunneling.[15,58] The layered structures of those charge tunable QDs can vary a lot, but basically they are modified versions based on p-i-n or Schottky diode.[36]

Figure 4.3 summarizes the measured T1 of QDs across several different samples at 6 Tesla. Red data points are from 30 nm tunneling barrier sample. Each dot measured are inside L3 cavity. On average, T1 in this sample is less than a few hundred nanoseconds at 6T. Blue and Magenta data sets are from 40 nm tunneling barrier samples. Though there are several data points showing T1 around 100 nanoseconds, it is safe to say that dots in 40 nm barrier can easily reach a few microseconds T1 lifetime. It is worth noting that etched surface of photonic structures can bring surface states and trapped charges that disturb spin properties. This may explain the several extreme low T1s measured on the 40 nm barrier sample. Also, the longest T1 measured on QD inside photonic cavity (1933 ns, blue data point) is comparable to the one measured on bulk dot inside planar DBR cavity without any etching (2097 ns, Magenta points). This might mean that for the dot located inside photonic structures but far away from the etched surface, the spin properties like T1 might still be protected. While 40 nm barrier samples clearly show advantage over 30 nm barrier sample in terms of T1 time, all those T1 data in the microsecond regime are much lower than the over 100 microseconds T1s at a few Tesla reported by several groups[12,15,56]. However, we also saw several groups reported several microseconds T1 at few Tesla,[69,71,93] which means our case might not be rare and T1 of QDs can vary a lot among different samples. At the time writing this dissertation, one work that compared QDs spin T1 of different

tunneling barrier is published online.[56] The authors reported three orders of magnitude difference of T1 between 37 nm barrier sample and 57 nm barrier sample.

4.4 Laser Induced Decay of T1

Red detuned lasers are commonly used to rotate solid state spins with optical transitions[54,72]. Usually the rotation lasers are 0.1 to several nanometers red detuned from the optical transitions of QDs spins. Broadband picosecond laser pulse and modulated CW laser with two sidebands are two most popular ways to rotate electron spin inside QDs. We observed serious decay of T1 brought by those off-resonant lasers which might explain the poor spin rotation fidelity we will present in next chapter.

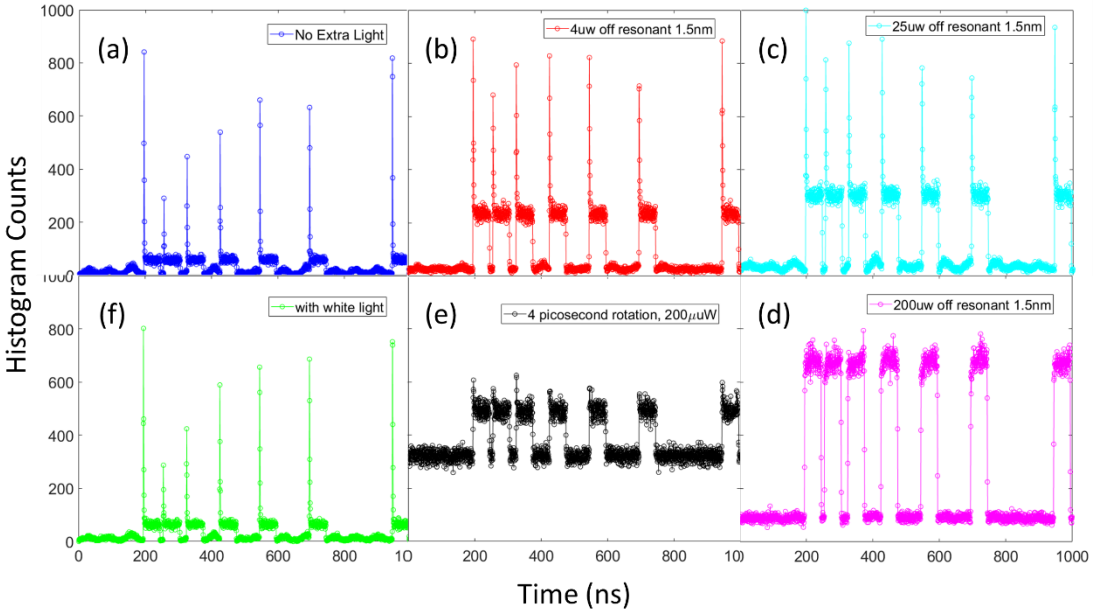

Figure 4.4 Raman signal of T1 measurement under different off-resonant light condition on the same dot of cavity 3113 fabricated from sample R161031F. In addition to pump laser used to perform T1 measurement, an additional off-resonant CW laser with different power was focused on the device surface ((a) to (d)). In (e), a picosecond rotation laser not synchronized with T1 pump laser pulses was used instead of CW laser in (a)-(d). In (f), a white light source was focused on the device surface instead of the CW lasers used in (a)-(e).

Figure 4.4 is the Raman signal generated by T1 pump laser pulse under different off-resonant laser condition. In addition to the resonant laser pulse train used to measure T1 as above, a CW laser that is 1.5 nm red detuned from the resonant laser is also focused on the QD from the same single mode fiber as the resonant laser. Figure 4.4(a) is the Raman signal without any off-resonant laser showing slow rising Raman spikes as the time delay increases. Also the background count plateau of Raman signal pulse, which is a balance between spin relaxation rate and laser initialization rate, is very low. When the off-resonant laser power is increased from 4 μW to 200 μW ((b) to (d)), the Raman spike of second pulse and background count increase sharply, indicating rapid worsening of T1 as the off-resonant laser power increases. In Figure 4.4(d), the spike, which is a signature of spin initialization, even disappears, indicating the laser initializing rate is smaller than the spin relaxation rate itself. Figure 4.4(e) is the case when a 200 μW picosecond laser was used instead of CW laser. Figure 4.4(f) is the case where a white light source, which is commonly used to image the sample surface, is used instead of the CW laser. The resulting T1 Raman is quite similar to that in (a), indicating the white light source has no effect on T1.

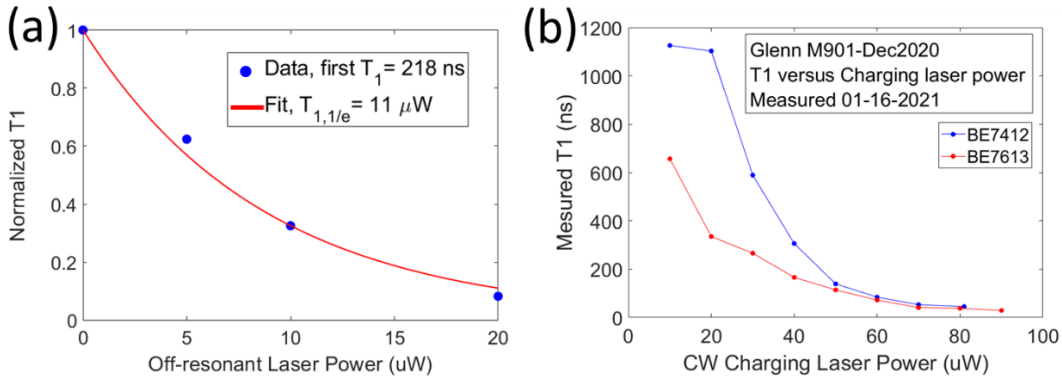

Figure 4.5 (a) Normalized T1 versus off-resonant laser power acquired using the same chip as in Figure 3.1 but on a different L3 cavity. The T1 without off-resonant laser was measured to be 218 ns. All T1 values were normalized to 218 ns. T1 measurement was performed at 6 Tesla. (b) The measured T1 of two bullseye cavities fabricated on sample.M918 (no diode structure) under different charging laser powers. The above band laser used here was a 780 nm diode laser.

Figure 4.5(a) plots the normalized spin T1 of cavity 5211 of sample R161031F versus the off-resonant CW laser power applied. The red line is the exponential decay fitting using $A * e\hat{}(P/\tau) + C$. The fitting result shows an off-resonant laser with 11 μW power could reduce the T1 to $1/e$. We measured the decay curve of several dots, and the $1/e$ decay power constants are around 10 μW.

Figure 4.5(b) is the measured T1 versus charging laser power of two dots from sample without diode structure (sample M918). Unlike those charge tunable dots buried inside PN diode, the charges inside those ungated dots are created by above band laser pumping. Excitons created by the above band laser would be captured by the dot. And due to each dot's local environment, only one of the electron-hole pair can stably stay inside the dot and the other would tunnel out of the dot, leaving the dot either negatively charged with one electron or positively charged with one hole. As mentioned above, this charging probability is very low, and in fact most of the dots in such sample are neutral. As shown in Figure 4.5(b), increasing charging laser would create more electrons to tunnel in and out of the dot, thus decreases the T1. However if the charging laser is too weak, which would reduce the time during which the dot is charged, the signal from the dot would become too weak to be measured. At larger charging laser power, the T1 of two different dots converges, indicating laser induced electron tunneling is the limiting factor of T1 at this time.

4.5 Conclusion

There are several important conclusions need to be made here: 1) We found 40 nm tunneling barrier samples have longer T1 lifetime (few microseconds) than the 30 nm barrier sample (a few hundred nanoseconds). This findings is also in line with

recently published paper.[56] 2) The measured T1 at few microseconds regime at 6 Tesla is comparable to several groups' reported T1 numbers but falls way behind the highest reported value, which are in the hundred microseconds regime. 3) We observed that T1 of electron spin could be strongly destroyed by off-resonant lasers, which are inevitably required to rotate the spin (see Chapter 5). This effect was only mentioned in one paper as laser induced depolarization[106], and the real mechanism behind is not clear yet.

From these two facts, it is safe to say that we need thicker tunnel barrier wafer to get longer T1. Also the mechanism leading to the laser induced T1 shortening needs to be understood and avoided.

Chapter 5: Coherent Control of an electron spin

5.1 *Chapter Introduction*

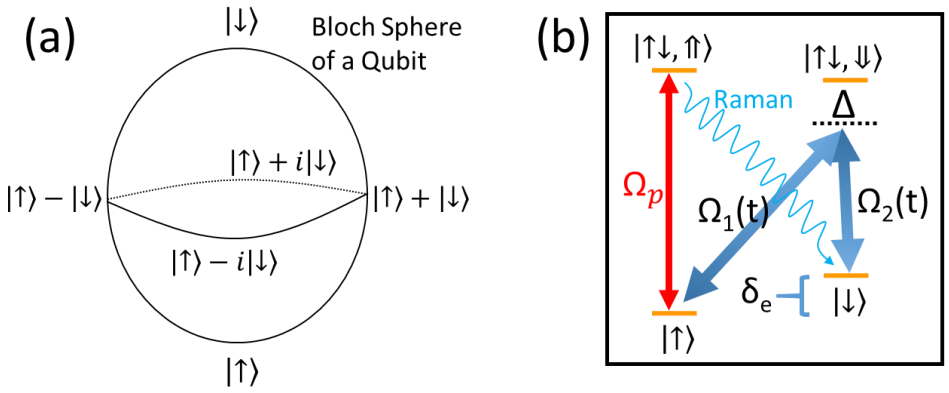

Figure 5.1 (a) Bloch sphere of a spin Qubit. (b) Illustration of spin rotation using optical fields that drive detuned transitions of QDs. In addition to the resonant CW laser (Ω_p) used to initialize and read out the spin state as in T1 measurement, two time varying laser fields $\Omega_1(t)$ and $\Omega_2(t)$, which are detuned from excited state by Δ, are used to rotate the spin between its two ground states.

The use of spin as a Qubit requires coherent rotation of the spin along its Bloch sphere[72]. This can be achieved by driving the three-level lambda system with two laser fields slight detuned from the excited states as shown in Figure 5.1(b).[72] Changing the power or the time duration of these two laser fields will coherently driving the system back and forth between its two ground states. The laser field needs to be detuned from the excited state to avoid pumping the system to its excited states. Combining with resonant laser initialization that has been introduced in Chapter 4, arbitrary rotation along the Bloch sphere with optical laser field can be achieved.[72] The difference of the frequency of these two laser fields should be equal to the ground spin states energy gap, which is the so-called two-photon resonance condition. To produce such optical field with two frequency, one can either use picosecond laser pulse from a Mode-Lock laser which features several tens of GHz bandwidth that is enough to cover the gap between

two ground states,[93,107] or one can use amplitude modulator to modulate CW laser[104] to produce two sidebands with frequency separation equal to the modulation frequency. We have developed both methods of spin rotation in our group, but this dissertation will primarily focus on picosecond laser technique. Another common method to rotate the spin is to use microwave to directly driving the transition between two spin ground states, which is widely used in the diamond spins[32] and requires the spin system to have large magnet dipole strength between its spin ground states. However, so far only one paper demonstrated electron spin resonance on InAs quantum dots using a macro coil.[108] And the electron spin resonance contrast in this paper is very small. Applying microwave rotation on QDs electron spin would be a quite exciting step because microwave is much simpler and more scalable and flexible than using lasers.

5.2 Ramsey Interferometry Experiment

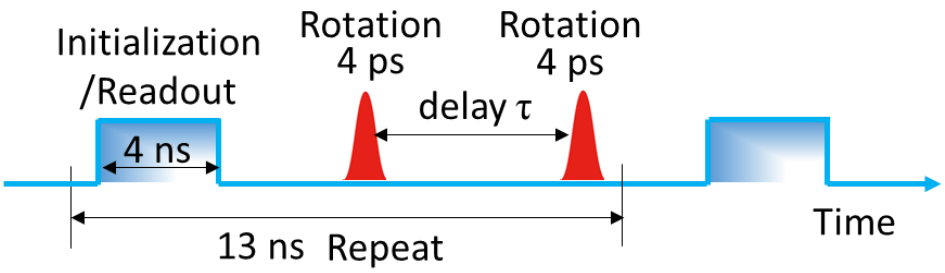

Figure 5.2 Laser pulse sequence of Ramsey Interference measurement. A 4 ns pulse created by EOM was used to perform spin initialization and readout as in T1 measurement. Two picosecond pulses from Mode-lock laser were used to rotate the spin along Bloch sphere. The period of the experiment (around 13.3 ns, 76 MHz) was determined by the repetition rate of Mode-lock laser. The delay between two rotation pulses is produced by a translation stage with several tens of picoseconds step size.

Figure 5.2 shows the pulse sequence used for Ramsey experiment.[34,107] A 4 ns pulse resonant with one of the optical transition created by an EOM was used to initialize the spin to either spin-up and spin-down state. Then two consecutive picosecond pulses with time delay between them were used to rotate the spin. The

degree of rotation of each pulse depends on their power and can be measured via Rabi experiment in next section. After being rotated by certain degree from up or down state by the first rotation pulse, the spin will start to process along the z-axis of the Bloch sphere with period determined by its ground state energy gap. Thus when the delay between two rotation pulses varies, the spin will reach different azimuth angle of the Bloch sphere. And depending on the location of spin at the time when second rotation pulse comes, the spin will be rotated to different location of the Bloch sphere. When the rotation pulse is a $\pi/2$ pulse, the final spin state will oscillate between up and down states, resulting oscillating Raman counts with maximum contrast. When the rotation pulse deviates from $\pi/2$ pulse, the contrast of Ramsey fringe will decrease.

To resolve individual optical transitions of QDs, we usually applied a magnetic field above 2 Tesla and up to 7 Tesla. This corresponds to a ground state energy gap ranging from 12 GHz to 40 GHz. The mode-lock laser we have can produce optical pulse with around 4 picoseconds width in time, corresponding to around 78 GHz and 0.22 nm in spectrum, which is enough to cover the energy gap of our dots at reasonable magnetic field strength.

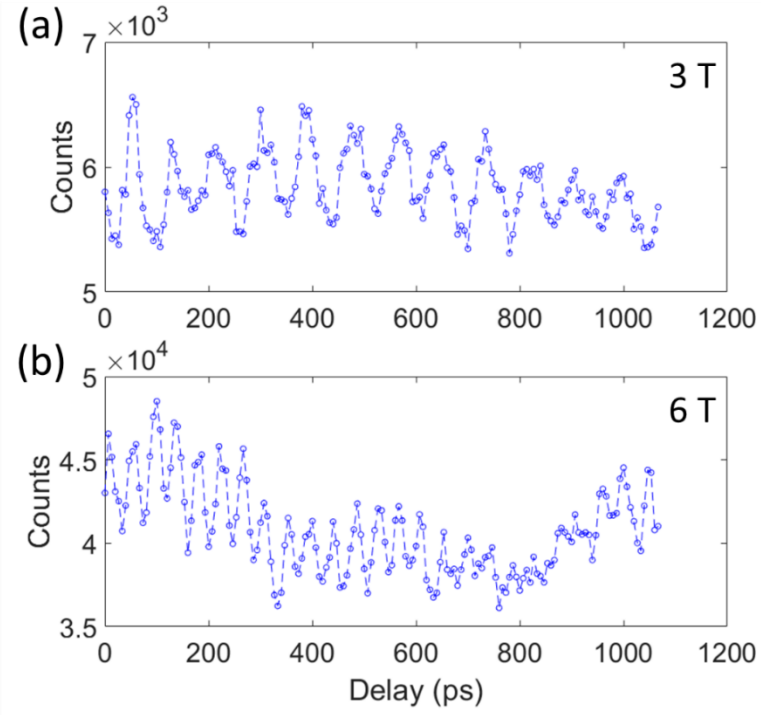

Figure 5.3 Ramsey fringes at two different magnetic field, 3 Tesla ((a)) and 6 Tesla ((b)). The rotation laser used here is a 4 picosecond laser with 1 nm red detuned from the excited states and with a measured average power of around 1 μW.

Figure 5.3 is the readout Raman counts on CCD camera when the delay between two rotation pulses is varied. The rotation laser is 1 nm red detuned from excited states with averaged power of around 1 μW at the entrance of cryostation. This rotation laser power was intentionally kept small to avoid laser induced depolarization described in Chapter 4, which means the rotation pulse was far from a π/2 pulse and the Ramsey fringe would be small. The Raman counts were directly read out on CCD camera mounted on the spectrometer since all light fields were different in wavelength. The Fourier transform of the oscillation data in (b) shows a principle frequency component at 23.3 GHz, matching the energy gap at 6 Tesla well. The frequency of (a) at 3 T is 11.5 GHz, which is half of that of (b) at 6 T as expected. The fringes in (a) and (b) shows decaying due to the limited coherence time of QDs electron spin ($T_2^* < 5\,ns$

[34,93,107,109] without any decoupling technique[110,111] and $T_2^* \sim \mu s$ [16] with spin echo or decoupling technique). Due to the length of our translation stage (300 mm) that was used to create the time delay between rotation pulses, longer time delay (> 2 ns) was not achievable. There is slow baseline drift of the Raman counts in Figure 5.3. This is due to the long term drifts of our setup, such as the drift of polarization in fiber and the drift of mechanical position of the piezo stages.

5.3 Rabi Oscillation Experiment

The spin rotation angle of the rotation laser depends on its energy area within each pulse. When the rotation laser power is increased, the spin would oscillate between spin-up and spin-down states, thus resulting oscillating Raman counts, so-called Rabi oscillation.[16,104] In Rabi oscillation experiment, the second rotation pulse in Figure 5.2 was removed and the power of first rotation pulse is varied while monitoring the Raman counts caused by initialization laser. Rabi experiment is a good way to determine $\pi/2$ pulse power and the rotation fidelity.

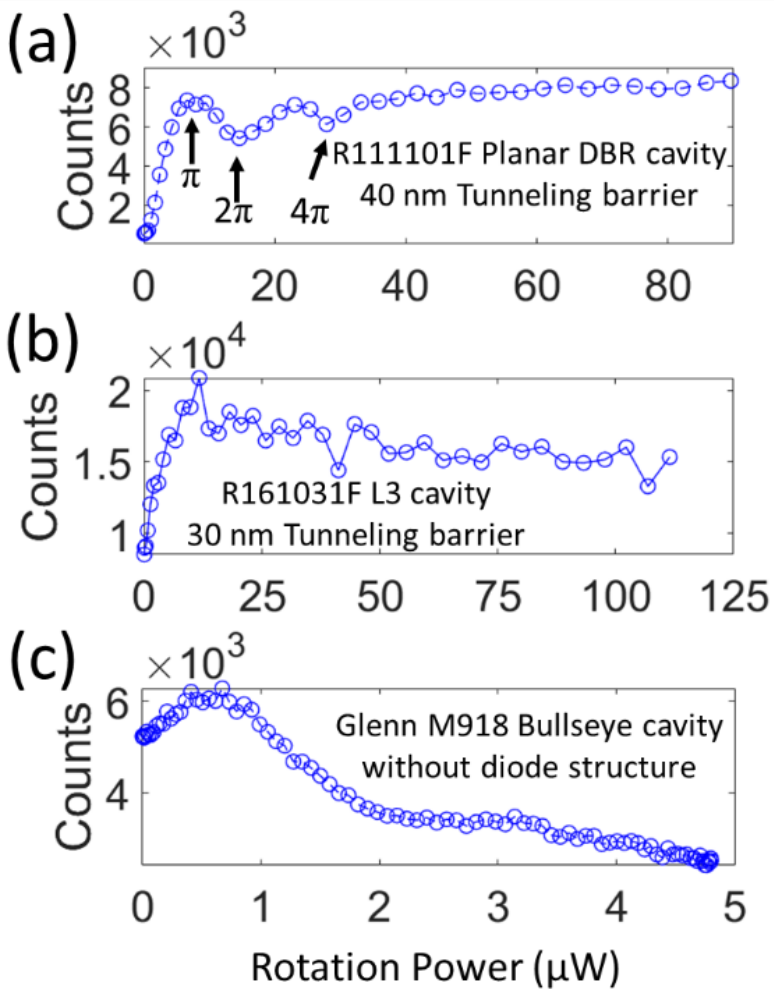

Figure 5.4 Raman counts versus picosecond pulse power used for rotation. (a) Rabi experiment performed on an electron spin of sample R111101F with 40 nm tunneling barrier. The picosecond laser is 1.3 nm red detuned from excited state. R111101F is a planar DBR cavity sample as previously mentioned. (b) Rabi experiment performed on electron spin inside 3113 L3 cavity of sample R161031F with tunneling barrier thickness of 30 nm. Rotation laser was 1.5 nm red detuned from excited state. (c) Rabi rotation performed on an electron spin inside a bullseye cavity 7613 of sample M918 without any diode structure. Picosecond laser was 1.5 nm detuned from excited state.

Figure 5.4 shows Rabi experiment performed on three different wafer using picosecond laser that was around 1.5 nm red detuned from the excited states. Figure 5.4(a) is the Rabi experiment data from an electron spin in a planar DBR sample with 40 nm tunneling barrier (R111101F). This is the best Rabi data we have got so far with

clear oscillations of several π. The increasing rotation power however caused off-resonant pumping and laser-induced depolarization, which stopped the Raman counts from reaching complete zero. Figure 5.4(b) is the data from an electron spin inside cavity 3113 of sample R161031F with a 30 nm tunneling barrier. Compared to (a), the rotation fidelity is even worse without a clear sinusoidal period. We believe this is due to the fact that the tunneling barrier is thinner than the sample used in (a), making sample more vulnerable to off-resonant laser related effects. Figure 5.4(c) is the Rabi rotation performed on an electron spin inside a Bullseye cavity (No.7614) from sample M918, which has no diode structure and relies on above band laser to charge the dot. The increasing rotation laser power in (c) causes the decrease of Raman count. This is very likely because the red detuned picosecond laser pushes the electron to tunnel out of the dot, thus leading to a decreased Raman count. The experiments in Figure 5.4 were performed mainly using a laser red detuned of around 1.5 nm. In fact, we have tried various detuning from less than 0.5 nm to 3 nm, but didn't see an improvement of rotation fidelity. We also tried Rabi rotation on multiple dots across different samples we have beyond the data shown in Figure 5.4, but they all suffered from off-resonant induced negative effects as is shown in Figure 5.4. So far people have reported up to 12π Rabi rotations with high oscillation contrast[16,107]. We believe the poor rotation fidelity of our sample is mainly due to the off-resonant laser induced depolarization.

5.4 Spin Rotation Using Sidebands of Modulated CW Laser

The rotation of spin basically involves two time varying laser fields that satisfy two photon resonance condition as Figure 5.1(b) shows. Picosecond laser is narrow in time thus is broaden in spectrum. This means not all frequency components of the

picosecond laser pulse is effective when being applied to rotate an electron spin. The spin rotation using picosecond laser pulse usually requires several tens of micro Watt to reach sample surface[34] and thus can be detrimental when the laser induced spin degeneracy effect exists. Those picosecond pulse is usually produced by optical methods like mode-lock, so it is difficult to produce picosecond pulses at arbitrary time with desired peak intensity. Alternatively, sidebands produced by modulating a CW laser can be used as rotation laser.[104] The frequency detuning between two sidebands equals to the intensity modulation frequency, while their center wavelength is the carrier laser frequency (Figure 5.5). Thus by varying the intensity modulation frequency, two photon resonance condition can be satisfied. The modulation of CW laser can be achieved by using those electro-optic modulator (EOM) or acoustic-optic modulator (AOM). The optical transmission of those modulator is determined by the electrical signal level sent to the RF port of the modulator. Thus the optical output of the modulator can be viewed as a print of the RF input signal. This allows us to produce complex rotation pulse sequences by simply preparing corresponding electrical signal using signal generators like AWG.

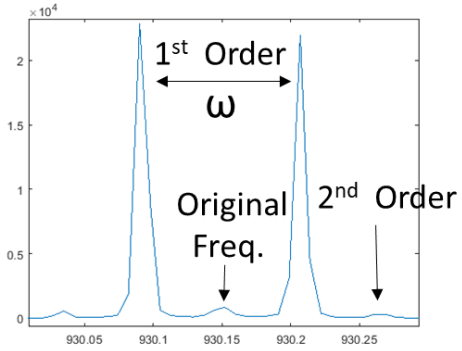

Figure 5.5 Spectrum of output laser from an electro-optic modulator. The input of the modulator is a CW laser with frequency indicated by Original Freq. The RF modulation frequency is ω, which equals to the distance between two first order sidebands. The bias of the modulator was tuned to minimize the component of carrier frequency and higher order sidebands. The elector-optic modulator we used was fiber based and had 20 GHz analog bandwidth, which was bought from EOSAPCE and ixblue.

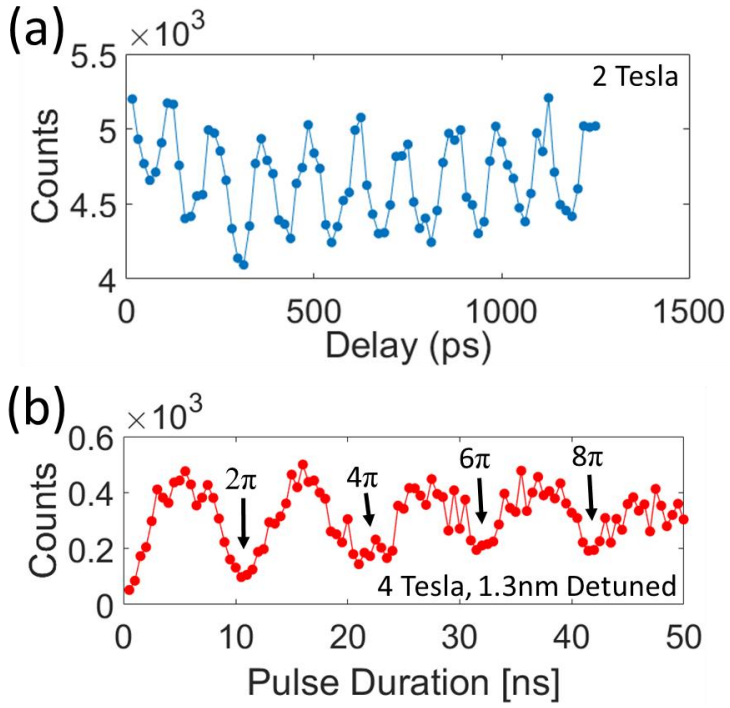

Figure 5.6 Spin rotation using sidebands of modulated CW laser. (a) Ramsey interference measured at 2 Tesla. (b) Rabi rotation with increasing rotation pulse length instead of increasing pulse peak intensity used in picosecond laser rotation experiment.

We developed the modulated CW technique in Waks group. This project was led by Dr. Farfurnik and here I will just briefly present some of the initial results. Figure 5.6 (a) is the Ramsey Interference experiment performed by modulated CW laser at 2 Tesla. It allows us to produce very long delay between two rotation pulses, which otherwise would be limited by the length of optical delay line used in picosecond rotation experiment in Figure 5.3. Figure 5.6(b) is the Rabi oscillation experiment with those modulated CW laser. Instead of increasing the laser peak intensity used in Figure 5.4, the length of rotation pulse was varied in Figure 5.6(b). Since the peak intensity was kept same in Figure 5.6(b), the laser induced spin degeneracy was less severe and thus gave us better oscillation contrast.

5.5 Conclusion

In conclusion, we have demonstrated Rabi rotation and Ramsey interference on different samples we have. 40 nm barrier sample has better rotation fidelity than the 30 nm barrier sample and the ungated sample. The low rotation fidelity is very likely due to the laser induced depolarization. Just as discussed in chapter 4, better sample with thicker tunneling barrier is necessary and needed. Also better photonic structures that can couple light more efficiently to the dots may help reduce the laser power that is needed to achieve $\pi/2$ and π rotation, thus increases the rotation fidelity. The using of modulated CW laser instead of picosecond pulse can also reduce the laser power needed to reach sample surface, thus reducing the laser induced effects.

Chapter 6: Conclusion and Outlooks

Here we summarize the content of this dissertation. In Chapter 2, various common photonic cavities were designed, scaled and optimized for InAs QDs emitting at 900 nm band. The designed cavities were fabricated and optically characterized, with comparison of their performance summarized in Table I. L3 cavity was found to have highest repeatable quality factor and small mode volume and was thus used in Chapter 3 for achieving strong coupling. Bullseye cavity was found to be bright and was thus used in Chapter 4 and 5 to explore spin properties. H1 cavity is theoretically the best candidate but was found difficult to be fabricated in reality. In Chapter 3, we achieved strong coupling between electron spin and L3 cavity, and demonstrated strong spin state dependent cavity resonant reflectivity. In Chapter 4, quantum dots electron spin T1 of different samples was measured and summarized. Few microseconds T1 were measured which are close to the values reported by several other groups but falls two order of magnitude behind the highest value reported so far. Samples with thicker tunneling barrier were found to have longer T1. Strong off-resonant laser induced shortening of T1 was observed. In Chapter 5, rotation of quantum dots electron spin using picosecond laser pulse was demonstrated. Both Ramsey interference and Rabi oscillation were presented. Sample with thicker tunneling barrier was found to have better rotation fidelity.

The near future work can be divided into two stages. In the first stage, sample with longer T1 and less prone to off-resonant laser needs to be developed. This can be achieved through close loop grow-measure-feedback process together with our

collaborators who provide us wafer. Second, the fabrication of H1 cavity, which in theory should have very high light coupling efficiency, needs to be perfected through multiple trials. This might be the key to reduce the off resonant laser-induced effects we are facing, through decreasing the laser power needed to reach sample surface. Third, mechanism behind the laser induced depolarization that destroys the spin properties, needs to be studied in depth since there are not much reports of such effects. After the goals of the first stage being achieved, which is to have quantum dots wafer with long T1 and immune to off-resonant laser depolarization, several important experiments can be performed, like deterministic spin-photon entanglement[102,112] and memory enhanced quantum comminication[32] which is based on such entanglement.

In the long run, to make quantum dots truly suitable for quantum information processing, methods to overcome inhomogeneous broadening, better coupling into single mode fiber, longer coherence time and higher gate fidelity need to be pushed forward.

Appendices

Appendix A. Experiment Setup

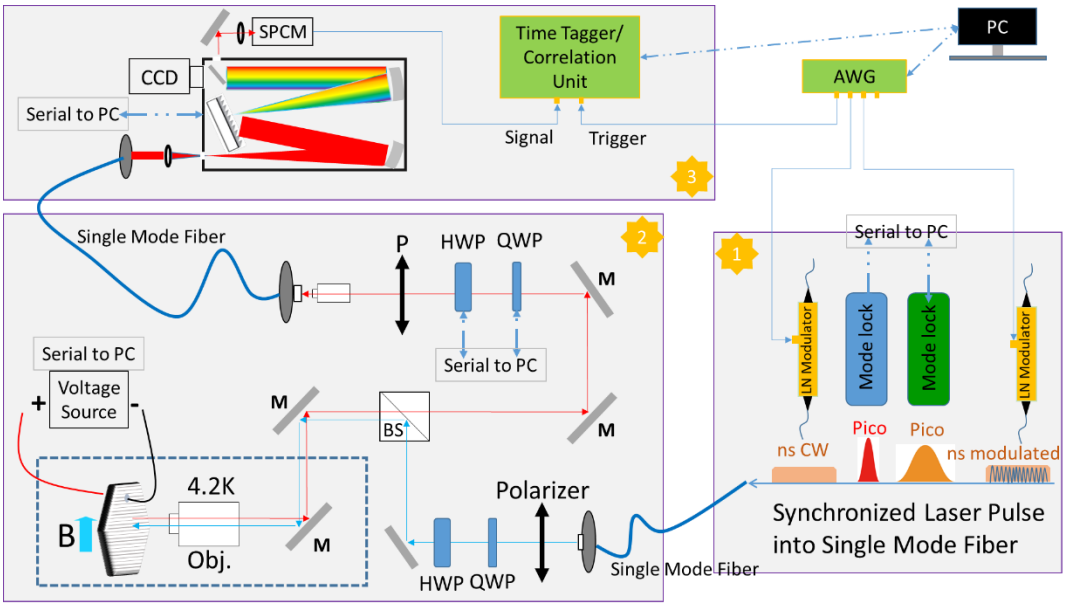

Figure 7.1 Scheme of optical setup. M: mirror, HWP: half-wave plate, QWP: quarter-wave plate, P: linear polarizer, BS: beam splitter, CCD: charge coupled device, SPCM: single photon counting module, AWG: arbitrary waveform generator, Obj.: objective lens, B: Magnetic field in Voigt Configuration, Pico: Picosecond laser pulse, CW: continuous wave laser, ns: nanosecond. The communication between instruments and PC was based on serial ports like RS232 and USB. Most of the instruments were automized and controlled using MATLAB.

The sample was mounted in a closed cycle liquid helium cryostat with a base temperature of ~4.3 K. A superconducting coil allowed us to apply a magnetic field of up to 9 T at a direction perpendicular to the sample growth (Voigt configuration). For photoluminescence measurements, we excited the InAs quantum dots with an above band laser (~890 nm) and collected their photoluminescence signal through the same objective lens with a N.A. of 0.68. For cavity reflectivity measurements, we excited the cavity with right-circularly polarized light and collected the left-circularly polarized component of the reflected signal using either a broadband light-emitting diode or a

narrow line width tunable laser for better spectral resolution. The rejection between the two cross-polarized components imposed by a pair of polarizers in the setup was larger than 10^5. The collected signal was then directed to a spectrometer with a grating resolution of less than 0.02 nm. For the optical pumping measurement, we simultaneously sent two narrow line width, tunable lasers into the cavity. For the time resolved measurement like T1, the Raman peak was filtered using spectrometer and then sent to SPCM for photon counting.

To produce picosecond pulse, mode-lock Ti-sapphire laser with tuning range from 700 nm to 1000 nm was used (Spectra Physics Tsunami). One end mirror of optical cavity of mode-lock laser was sit on a motor and piezo stage, allowing itself to be triggered and synchronized with external gate signal. The pulse width of picosecond laser was measured to be around 4 ps using an auto-correlator. To produce arbitrary laser pulse on the nanosecond regime, fiber based electro-optic modulator (30 GHz bandwidth from EOSPACE and 20 GHz bandwidth from ixblue) was used with the optical pulse printed by the microwave (MW) electrical pulse generated by Arbitrary Waveform Generator (Keysight M8195A). To produce time delay between picosecond pulses, a beam splitter was first used to split the optical pulse into two paths, with one of the paths going through an optical delay line formed by a retro reflector sitting on a linear translation stage with 300 mm travel distance from Thorlabs. And then the two optical pulses with time delay were combined by a second beam splitter and focused into the same single mode fiber.

Appendix B. Semiconductor Fabrication

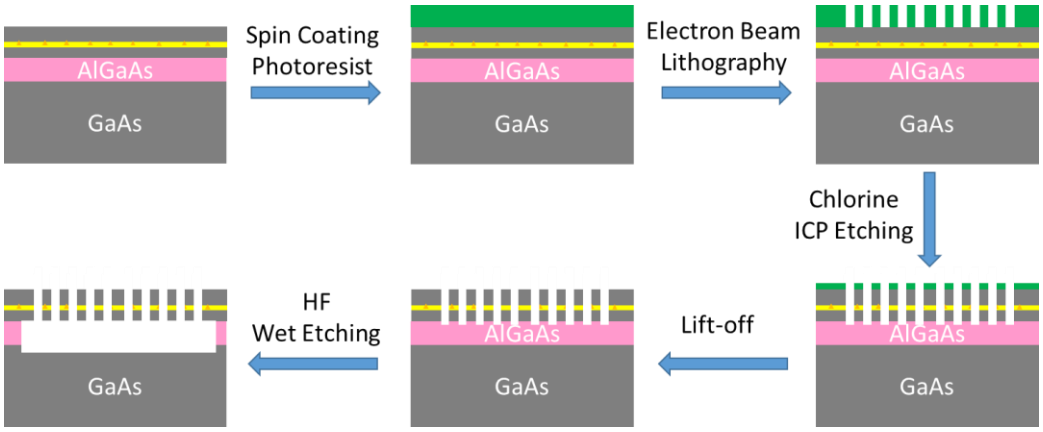

Figure 7.2 Semiconductor fabrication flow chart of GaAs.

The GaAs diode-gated InAs quantum dot material was grown by a molecular beam epitaxy process similar to that used by Carter et al.[54] We spin-coated a positive photoresist (ZEP520A) with a thickness of ~500 nm on the sample surface. L3 cavities with a lattice constant of 236 nm and hole radius of 70 nm were patterned into the photoresist by electron beam lithography and then transferred to the diode by inductively coupled plasma dry etching. A suspended cavity membrane with a thickness of 180 nm was formed after we wet-etched away the n-type AlGaAs sacrificial layer using hydrofluoric acid. Electrical contacts were made to the top and bottom of the sample with indium and conductive epoxy, and the sample was glued to a chip carrier.

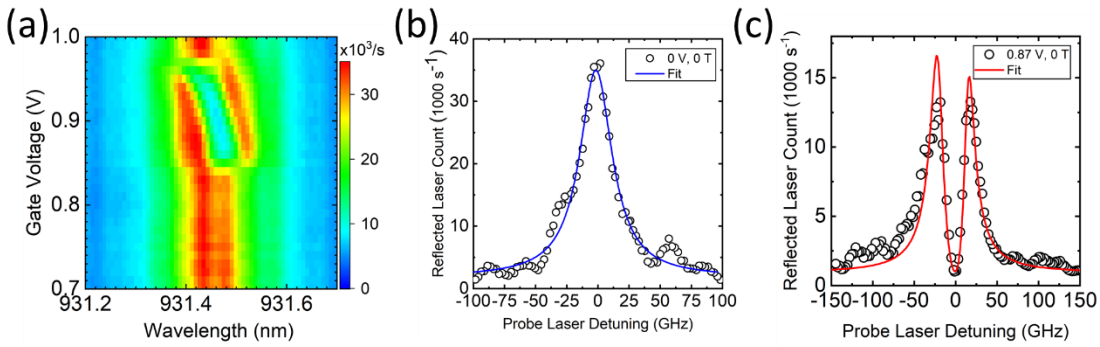

Figure 7.3 Characterization of the strongly coupled quantum dot-cavity system at 0 T. (a) Reflectivity spectrum excited by broadband LED at different gate. The color represents the counts on the CCD camera. (b) The reflectivity spectrum of the bare cavity (black circles) fitted with a Lorentzian line shape (solid blue line). (c) The reflectivity spectrum of the cavity at 0.87 V. The red solid line is the theoretical fitting of the experimental data (black circles).

To extract the cavity loss κ, we fine scanned the cavity reflectivity using a tunable narrow linewidth laser (Figure 7.3(b), black circles). The voltage was set to 0 V, which eliminated all the quantum dots emission (bare cavity). We fit the spectra to a Lorentzian shape (blue line in Figure 7.3(b)) and extracted a cavity decay rate of $\kappa/2\pi = 31.79 \pm 1.9\ GHz$, which is equivalent to a cavity quality factor of Q ~10,000.

To measure the coupling strength between the charged quantum dot and the cavity at 0 T, we scanned the cavity reflectivity at 0.87 V (Figure 7.3 (c), black circles). We fit the coupled cavity-dot spectrum in Figure 7.3 (c) to equation S1[26,113]:

$$R = B + S/\left|(-i\Delta\omega + \frac{\kappa}{2} + \frac{g^2}{(-i(\Delta\omega-\delta)+\gamma)})\right|^2, \qquad \text{(S1)}$$

where g is the coupling strength between the quantum dot and the cavity, γ is the dipole decay rate of the quantum dot, $\Delta\omega$ is the detuning between the laser and the cavity, and δ is the detuning between the quantum dot and the cavity (red line, Figure 7.3 (c)). B and S are fitting parameters accounting for the spectrum background and

scaling factor, respectively. From the numerical fit we extracted $g/2\pi = 18.67 \pm 0.35$ GHz and $\gamma/2\pi = 1.78 \pm 0.70$ GHz, which gave us an atom-cavity cooperativity of $C = 2g^2/\kappa\gamma = 12.35$. The linewidth of our dot is larger than the transform limit, possibly due to the fact that the quantum dots are close to the etching surface compared with bulk quantum dots or those fabricated within micropillars.[41,114]

We note that the existence of alignment imperfection (inevitable Fabry-Perot effect among optical elements of the experiment setup) broadened the linewidth of the left peak of Figure 7.3 (c) and the fitting tended to follow the broadened feature but couldn't fit well with the reflection dip depth. To extract an accurate cooperativity, we gave larger weight to the three data points at the center of the reflectivity spectrum of Figure 7.3(c) to ensure the fitting curve can fit well with the reflection dip because cooperativity is determined by the depth of the reflection dip. We also gave larger weight to the three data points at the center of reflection dip of Figure 3.5(b) because of the same reason.

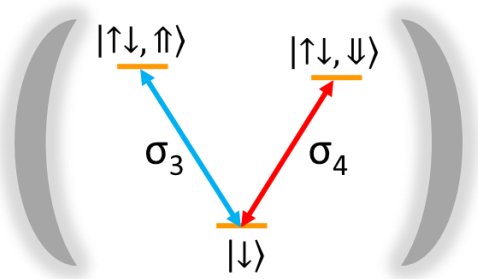

Figure 7.4 The energy-level diagram of a three-level V-scheme system coupled to a cavity, simplified from the four-energy level scheme of a charged quantum dot, shown in Figure 1.1(a).

To get $R_{up}(\omega)$ and $R_{down}(\omega)$, we numerically calculated the system density matrix ρ at steady state governed by $d\rho/dt = -i/\hbar[\hat{H}, \rho] + \hat{L}\rho$, where $\hat{H}$ is the Hamiltonian of this coupled quantum dot-cavity system when the spin is in pure $|\uparrow\rangle$ or $|\downarrow\rangle$ state and $\hat{L}$ is Liouvillian superoperator used to model all nonunitary Markovian processes in this system. R_{up} and R_{down} are proportional to $Tr(\rho_{ss}(\omega)\hat{a}^{\dagger}\hat{a})$, where ρ_{ss} is the system density matrix at steady state and $\hat{a}$ is the annihilation operator of the cavity field. The spectrum of Figure 3.5 (a) and (b) can be fit using $R_m = S * (P_{up} * Tr(\rho_{ss,\uparrow}(\omega)\hat{a}^{\dagger}\hat{a}) + (1 - P_{up}) * Tr(\rho_{ss,\downarrow}(\omega)\hat{a}^{\dagger}\hat{a})) + B$. S and B are the fitting parameters account for scaling and background.

When the spin population is in spin-down state, the energy level structure of the charged quantum dot can by simplified as a three level V-scheme system coupled to a

cavity, as shown in Figure 7.4. The Hamiltonian of this system in the rotation frame with respect to the probe laser frequency can be written as:

$$\hat{H} = \hbar(\omega_c - \omega)\hat{a}^\dagger\hat{a} + \hbar(\omega_x - \omega)\hat{\sigma}_3^\dagger\hat{\sigma}_3 + \hbar(\omega_x - \Delta_h - \omega)\hat{\sigma}_4^\dagger\hat{\sigma}_4 + ig_3\hbar\left(\hat{a}\hat{\sigma}_3^\dagger - \hat{\sigma}_3\hat{a}^\dagger\right) + g_4\hbar\left(\hat{a}\hat{\sigma}_4^\dagger + \hat{\sigma}_4\hat{a}^\dagger\right), \quad \text{(S2)}$$

in which $\hat{\sigma}_3$ and $\hat{\sigma}_4$ are the lowering operators of transitions σ3 and σ4, respectively, $\hat{a}$ is the annihilation operator of the cavity field, g_3 and g_4 are the coupling strength between σ3 and σ4 with the cavity, respectively, ω_c, ω_x, $(\omega_x - \Delta_h)$ and ω are the frequency of the cavity, transition σ3, transition σ4, and the laser, respectively, and Δ_h is the Zeeman splitting between the two excited states.

The Liouvillian superoperator $\hat{L}$, which accounts for the decay of the cavity field, spontaneous emission, and dephasing of the excited trion states, can be written as:

$$\hat{L} = \kappa D(\hat{a}) + \gamma_3 D(\hat{\sigma}_3) + \gamma_4 D(\hat{\sigma}_4) + 2\gamma_{d3} D\left(\hat{\sigma}_3^\dagger\hat{\sigma}_3\right) + 2\gamma_{d4} D\left(\hat{\sigma}_4^\dagger\hat{\sigma}_4\right), \quad \text{(S3)}$$

in which $D(\hat{O})\rho = \hat{O}\rho\hat{O}^\dagger - 1/2\hat{O}^\dagger\hat{O}\rho - 1/2\rho\hat{O}^\dagger\hat{O}$ is the general Linblad form operator for an operator $\hat{O}$, the coefficients $\kappa, \gamma_3, \gamma_4, \gamma_{d3}$, and γ_{d4} are the cavity loss, spontaneous emission rates of σ3 and σ4, and the pure dephasing rates of σ3 and σ4, respectively.

When the spin population is in spin-up state, the quantum dot can only couple to cavity through σ2 and σ1, which are largely detuned. In this case, the system can be simplified as a bare cavity without any coupling to the quantum dot, which is equivalent to setting g_3 and g_4 to be 0 in equation (S2).

We first fit Figure 3.5(b) using the above numerical model. We already determined $\kappa/2\pi$ to be 31.79 GHz from Figure 7.3(b). $\gamma_3/2\pi$ and $\gamma_4/2\pi$ were set to 0.1 GHz.[115] We also imposed $g_3^2 + g_4^2 = g^2$, in which g is the coupling strength between the quantum dot and cavity at 0 T and 0.87 V, which was extracted in Figure 3.5(c). This constraint relation comes from the fact that the dipole transition between the excited state and ground state at 0 T ($\sigma_\pm$) could be written as $\sigma_\pm = \hat{\sigma}_4 \pm i\hat{\sigma}_3$. When multiple dipole transitions are coupled to a cavity, the overall effective coupling strength g is related to individual coupling strength g_i by $g^2 = \sum g_i^2$.[116] We used the rest system parameters *S*, *B*, ω_c, ω_x, g_3, γ_{d3}, and γ_{d4} as free fitting parameters. We got $g_3/2\pi = 7.2\ GHz$, $g_4/2\pi = 17.2\ GHz$, $\gamma_{d3}/2\pi = 3.1\ GHz$, $\gamma_{d4}/2\pi = 1.4\ GHz$. P_{up} was determined to be less than 0.02 by 95% confidential bound. The fitting result is further discussed in the main text.

With the value of g_3, g_4, γ_{d3}, and γ_{d4} fixed from fitting of Figure 3.5(c), we then fit the spectrum of Figure 3.5(b). The spin population at thermal equilibrium was determined to be $P_{up} = 0.52 \pm 0.04$.

Bibliography

(1) Cirac, J. I.; Zoller, P.; Kimble, H. J.; Mabuchi, H. Quantum State Transfer and Entanglement Distribution among Distant Nodes in a Quantum Network. *Phys. Rev. Lett.* **1997**, *78* (16), 3221–3224.

(2) Kimble, H. J. The Quantum Internet. *Nat. 2008 4537198* **2008**.

(3) Cirac, J. I.; Ekert, A. K.; Huelga, S. F.; Macchiavello, C. Distributed Quantum Computation over Noisy Channels. *Phys. Rev. A* **1999**, *59* (6), 4249–4254.

(4) Cho, J.; Lee, H. W. Generation of Atomic Cluster States through the Cavity Input-Output Process. *Phys. Rev. Lett.* **2005**.

(5) Ritter, S.; Nölleke, C.; Hahn, C.; Reiserer, A.; Neuzner, A.; Uphoff, M.; Mücke, M.; Figueroa, E.; Bochmann, J.; Rempe, G. An Elementary Quantum Network of Single Atoms in Optical Cavities. *Nature* **2012**.

(6) Duan, L. M.; Kimble, H. J. Scalable Photonic Quantum Computation through Cavity-Assisted Interactions. *Phys. Rev. Lett.* **2004**.

(7) Bonato, C.; Haupt, F.; Oemrawsingh, S. S. R.; Gudat, J.; Ding, D.; van Exter, M. P.; Bouwmeester, D. CNOT and Bell-State Analysis in the Weak-Coupling Cavity QED Regime. *Phys. Rev. Lett.* **2010**, *104* (16), 160503.

(8) Reiserer, A.; Kalb, N.; Rempe, G.; Ritter, S. A Quantum Gate between a Flying Optical Photon and a Single Trapped Atom. *Nature* **2014**.

(9) Reiserer, A.; Kalb, N.; Rempe, G.; Ritter, S. A Quantum Gate between a Flying Optical Photon and a Single Trapped Atom. *Nature* **2014**, *508* (7495), 237–240.

(10) Englund, D.; Faraon, A.; Zhang, B.; Yamamoto, Y.; Vu?kovi?, J. Generation and Transfer of Single Photons on a Photonic Crystal Chip. *Opt. Express* **2007**, *15* (9), 5550.

(11) Faraon, A.; Majumdar, A.; Englund, D.; Kim, E.; Bajcsy, M.; Vučković, J. Integrated Quantum Optical Networks Based on Quantum Dots and Photonic Crystals. *New J. Phys.* **2011**.

(12) Kroutvar, M.; Ducommun, Y.; Heiss, D.; Bichler, M.; Schuh, D.; Abstreiter, G.; Finley, J. J. Optically Programmable Electron Spin Memory Using Semiconductor Quantum Dots. *Nature* **2004**, *432* (7013), 81–84.

(13) Warburton, R. J. Single Spins in Self-Assembled Quantum Dots. *Nat. Mater.* **2013**, *12* (6), 483–493.

(14) Petroff, P. M.; Lorke, A.; Imamoglu, A. Epitaxially Self-Assembled Quantom Dots. *Phys. Today* **2001**, *54* (5), 46–52.

(15) Lu, C. Y.; Zhao, Y.; Vamivakas, A. N.; Matthiesen, C.; Fält, S.; Badolato, A.; Atatüre, M. Direct Measurement of Spin Dynamics in InAs/GaAs Quantum Dots Using Time-Resolved Resonance Fluorescence. *Phys. Rev. B - Condens.*

Matter Mater. Phys. **2010**.

(16) Press, D.; De Greve, K.; McMahon, P. L.; Ladd, T. D.; Friess, B.; Schneider, C.; Kamp, M.; Höfling, S.; Forchel, A.; Yamamoto, Y. Ultrafast Optical Spin Echo in a Single Quantum Dot. *Nat. Photonics* **2010**, *4* (6), 367–370.

(17) Santori, C.; Fattal, D.; Vučković, J.; Solomon, G. S.; Yamamoto, Y. Indistinguishable Photons from a Single-Photon Device. *Nature* **2002**.

(18) Senellart, P.; Solomon, G.; White, A. High-Performance Semiconductor Quantum-Dot Single-Photon Sources. *Nature Nanotechnology*. 2017.

(19) Somaschi, N.; Giesz, V.; De Santis, L.; Loredo, J. C.; Almeida, M. P.; Hornecker, G.; Portalupi, S. L.; Grange, T.; Antón, C.; Demory, J.; et al. Near-Optimal Single-Photon Sources in the Solid State. *Nat. Photonics* **2016**, *10* (5), 340–345.

(20) Wang, H.; He, Y. M.; Chung, T. H.; Hu, H.; Yu, Y.; Chen, S.; Ding, X.; Chen, M. C.; Qin, J.; Yang, X.; et al. Towards Optimal Single-Photon Sources from Polarized Microcavities. *Nat. Photonics* **2019**.

(21) Faraon, A.; Fushman, I.; Englund, D.; Stoltz, N.; Petroff, P.; Vučković, J. Coherent Generation of Non-Classical Light on a Chip via Photon-Induced Tunnelling and Blockade. *Nat. Phys.* **2008**.

(22) Tiurev, K.; Appel, M. H.; Mirambell, P. L.; Lauritzen, M. B.; Tiranov, A.; Lodahl, P.; Sørensen, A. S. High-Fidelity Multi-Photon-Entangled Cluster State with Solid-State Quantum Emitters in Photonic Nanostructures. *arXiv*. 2020.

(23) Miao, C.; Fang, S. D.; Dong, P.; Yang, M.; Cao, Z. L. Generation of Large Scale GHZ States with the Interactions of Photons and Quantum-Dot Spins. *Laser Phys. Lett.* **2018**.

(24) Lodahl, P.; Mahmoodian, S.; Stobbe, S. Interfacing Single Photons and Single Quantum Dots with Photonic Nanostructures. *Rev. Mod. Phys.* **2015**, *87* (2), 347–400.

(25) Imamoglu, A.; Awschalom, D. D.; Burkard, G.; DiVincenzo, D. P.; Loss, D.; Sherwin, M.; Small, A. Quantum Information Processing Using Quantum Dot Spins and Cavity Qed. *Phys. Rev. Lett.* **1999**.

(26) Waks, E.; Vuckovic, J. Dipole Induced Transparency in Drop-Filter Cavity-Waveguide Systems. *Phys. Rev. Lett.* **2006**, *96* (15), 153601.

(27) Chang, D. E.; Sørensen, A. S.; Demler, E. A.; Lukin, M. D. A Single-Photon Transistor Using Nanoscale Surface Plasmons. *Nat. Phys.* **2007**.

(28) Hu, C. Y.; Young, A.; O'Brien, J. L.; Munro, W. J.; Rarity, J. G. Giant Optical Faraday Rotation Induced by a Single-Electron Spin in a Quantum Dot: Applications to Entangling Remote Spins via a Single Photon. *Phys. Rev. B - Condens. Matter Mater. Phys.* **2008**.

(29) Li, Y.; Aolita, L.; Chang, D. E.; Kwek, L. C. Robust-Fidelity Atom-Photon

Entangling Gates in the Weak-Coupling Regime. *Phys. Rev. Lett.* **2012**.

(30) Nemoto, K.; Trupke, M.; Devitt, S. J.; Stephens, A. M.; Scharfenberger, B.; Buczak, K.; Nöbauer, T.; Everitt, M. S.; Schmiedmayer, J.; Munro, W. J. Photonic Architecture for Scalable Quantum Information Processing in Diamond. *Phys. Rev. X* **2014**.

(31) Wang, T. J.; Song, S. Y.; Long, G. L. Quantum Repeater Based on Spatial Entanglement of Photons and Quantum-Dot Spins in Optical Microcavities. *Phys. Rev. A - At. Mol. Opt. Phys.* **2012**.

(32) Bhaskar, M. K.; Riedinger, R.; Machielse, B.; Levonian, D. S.; Nguyen, C. T.; Knall, E. N.; Park, H.; Englund, D.; Lončar, M.; Sukachev, D. D.; et al. Experimental Demonstration of Memory-Enhanced Quantum Communication. *Nature* **2020**.

(33) Sun, S.; Kim, H.; Luo, Z.; Solomon, G. S.; Waks, E. A Single-Photon Switch and Transistor Enabled by a Solid-State Quantum Memory. *Science (80-.).* **2018**.

(34) Sun, S.; Kim, H.; Solomon, G. S.; Waks, E. A Quantum Phase Switch between a Single Solid-State Spin and a Photon. *Nat. Nanotechnol.* **2016**, *11* (6), 539–544.

(35) Androvitsaneas, P.; Young, A. B.; Schneider, C.; Maier, S.; Kamp, M.; Höfling, S.; Knauer, S.; Harbord, E.; Hu, C. Y.; Rarity, J. G.; et al. Charged Quantum Dot Micropillar System for Deterministic Light-Matter Interactions. *Phys. Rev. B* **2016**, *93* (24), 241409.

(36) Lagoudakis, K. G.; Fischer, K.; Sarmiento, T.; Majumdar, A.; Rundquist, A.; Lu, J.; Bajcsy, M.; Vučković, J. Deterministically Charged Quantum Dots in Photonic Crystal Nanoresonators for Efficient Spin–Photon Interfaces. *New J. Phys.* **2013**, *15* (11), 113056.

(37) Arnold, C.; Demory, J.; Loo, V.; Lemaître, A.; Sagnes, I.; Glazov, M.; Krebs, O.; Voisin, P.; Senellart, P.; Lanco, L. Macroscopic Rotation of Photon Polarization Induced by a Single Spin. *Nat. Commun.* **2015**, *6* (1), 6236.

(38) Drexler, H.; Leonard, D.; Hansen, W.; Kotthaus, J. P.; Petroff, P. M. Spectroscopy of Quantum Levels in Charge-Tunable InGaAs Quantum Dots. *Phys. Rev. Lett.* **1994**, *73* (16), 2252–2255.

(39) Warburton, R. J.; Schäflein, C.; Haft, D.; Bickel, F.; Lorke, A.; Karrai, K.; Garcia, J. M.; Schoenfeld, W.; Petroff, P. M. Optical Emission from a Charge-Tunable Quantum Ring. *Nature* **2000**, *405* (6789), 926–929.

(40) Berezovsky, J.; Mikkelsen, M. H.; Gywat, O.; Stoltz, N. G.; Coldren, L. A.; Awschalom, D. D. Nondestructive Optical Measurements of a Single Electron Spin in a Quantum Dot. *Science* **2006**, *314* (5807), 1916–1920.

(41) Giesz, V.; Somaschi, N.; Hornecker, G.; Grange, T.; Reznychenko, B.; De Santis, L.; Demory, J.; Gomez, C.; Sagnes, I.; Lemaître, A.; et al. Coherent Manipulation of a Solid-State Artificial Atom with Few Photons. *Nat.*

Commun. **2016**, *7* (1), 11986.

(42) Kuhlmann, A. V.; Houel, J.; Ludwig, A.; Greuter, L.; Reuter, D.; Wieck, A. D.; Poggio, M.; Warburton, R. J. Charge Noise and Spin Noise in a Semiconductor Quantum Device. *Nat. Phys.* **2013**, *9* (9), 570–575.

(43) Petroff, P. M.; DenBaars, S. P. MBE and MOCVD Growth and Properties of Self-Assembling Quantum Dot Arrays in III-V Semiconductor Structures. *Superlattices Microstruct.* **1994**.

(44) Cusack, M.; Briddon, P.; Jaros, M. Electronic Structure of InAs/GaAs Self-Assembled Quantum Dots. *Phys. Rev. B - Condens. Matter Mater. Phys.* **1996**.

(45) Ithurria, S.; Tessier, M. D.; Mahler, B.; Lobo, R. P. S. M.; Dubertret, B.; Efros, A. L. Colloidal Nanoplatelets with Two-Dimensional Electronic Structure. *Nat. Mater.* **2011**.

(46) Hanson, R.; Kouwenhoven, L. P.; Petta, J. R.; Tarucha, S.; Vandersypen, L. M. K. Spins in Few-Electron Quantum Dots. *Rev. Mod. Phys.* **2007**.

(47) Petta, J. R.; Johnson, A. C.; Taylor, J. M.; Laird, E. A.; Yacoby, A.; Lukin, M. D.; Marcus, C. M.; Hanson, M. P.; Gossard, A. C. Applied Physics: Coherent Manipulation of Coupled Electron Spins in Semiconductor Quantum Dots. *Science (80-.).* **2005**.

(48) Bluhm, H.; Foletti, S.; Neder, I.; Rudner, M.; Mahalu, D.; Umansky, V.; Yacoby, A. Dephasing Time of GaAs Electron-Spin Qubits Coupled to a Nuclear Bath Exceeding 200 Μs. *Nat. Phys.* **2011**, *7* (2), 109–113.

(49) Golovach, V. N.; Khaetskii, A.; Loss, D. Phonon-Induced Decay of the Electron Spin in Quantum Dots. *Phys. Rev. Lett.* **2004**.

(50) Scarlino, P.; Kawakami, E.; Stano, P.; Shafiei, M.; Reichl, C.; Wegscheider, W.; Vandersypen, L. M. K. Spin-Relaxation Anisotropy in a GaAs Quantum Dot. *Phys. Rev. Lett.* **2014**.

(51) Lee, C. M.; Buyukkaya, M. A.; Harper, S.; Aghaeimeibodi, S.; Richardson, C. J. K.; Waks, E. Bright Telecom-Wavelength Single Photons Based on a Tapered Nanobeam. *Nano Lett.* **2021**.

(52) Sun, S.; Kim, H.; Solomon, G. S.; Waks, E. A Quantum Phase Switch between a Single Solid-State Spin and a Photon. *Nat. Nanotechnol.* **2016**.

(53) Pinotsi, D.; Fallahi, P.; Miguel-Sanchez, J.; Imamoglu, A. Resonant Spectroscopy on Charge Tunable Quantum Dots in Photonic Crystal Structures. *IEEE J. Quantum Electron.* **2011**, *47* (11), 1371–1374.

(54) Carter, S. G.; Sweeney, T. M.; Kim, M.; Kim, C. S.; Solenov, D.; Economou, S. E.; Reinecke, T. L.; Yang, L.; Bracker, A. S.; Gammon, D. Quantum Control of a Spin Qubit Coupled to a Photonic Crystal Cavity. *Nat. Photonics* **2013**.

(55) Bayer, M.; Ortner, G.; Stern, O.; Kuther, A.; Gorbunov, A. A.; Forchel, A.; Hawrylak, P.; Fafard, S.; Hinzer, K.; Reinecke, T. L.; et al. Fine Structure of

Neutral and Charged Excitons in Self-Assembled In(Ga)As/(Al)GaAs Quantum Dots. *Phys. Rev. B* **2002**, *65* (19), 195315.

(56) Gillard, G.; Griffiths, I. M.; Ragunathan, G.; Ulhaq, A.; McEwan, C.; Clarke, E.; Chekhovich, E. A. Fundamental Limits of Electron and Nuclear Spin Qubit Lifetimes in an Isolated Self-Assembled Quantum Dot. *npj Quantum Inf.* **2021**.

(57) Löbl, M. C.; Spinnler, C.; Javadi, A.; Zhai, L.; Nguyen, G. N.; Ritzmann, J.; Midolo, L.; Lodahl, P.; Wieck, A. D.; Ludwig, A.; et al. Radiative Auger Process in the Single-Photon Limit. *Nat. Nanotechnol.* **2020**.

(58) Najer, D.; Söllner, I.; Sekatski, P.; Dolique, V.; Löbl, M. C.; Riedel, D.; Schott, R.; Starosielec, S.; Valentin, S. R.; Wieck, A. D.; et al. A Gated Quantum Dot Strongly Coupled to an Optical Microcavity. *Nature* **2019**.

(59) Pedersen, F. T.; Wang, Y.; Olesen, C. T.; Scholz, S.; Wieck, A. D.; Ludwig, A.; Löbl, M. C.; Warburton, R. J.; Midolo, L.; Uppu, R.; et al. Near Transform-Limited Quantum Dot Linewidths in a Broadband Photonic Crystal Waveguide. *ACS Photonics* **2020**.

(60) Kuhlmann, A. V.; Prechtel, J. H.; Houel, J.; Ludwig, A.; Reuter, D.; Wieck, A. D.; Warburton, R. J. Transform-Limited Single Photons from a Single Quantum Dot. *Nat. Commun.* **2015**.

(61) Kapon, E.; Pelucchi, E.; Watanabe, S.; Malko, A.; Baier, M. H.; Leifer, K.; Dwir, B.; Michelini, F.; Dupertuis, M. A. Site- And Energy-Controlled Pyramidal Quantum Dot Heterostructures. In *Physica E: Low-Dimensional Systems and Nanostructures*; 2004.

(62) Ishikawa, T.; Nishimura, T.; Kohmoto, S.; Asakawa, K. Site-Controlled InAs Single Quantum-Dot Structures on GaAs Surfaces Patterned by in Situ Electron-Beam Lithography. *Appl. Phys. Lett.* **2000**.

(63) Kim, J. H.; Aghaeimeibodi, S.; Richardson, C. J. K.; Leavitt, R. P.; Englund, D.; Waks, E. Hybrid Integration of Solid-State Quantum Emitters on a Silicon Photonic Chip. *Nano Lett.* **2017**.

(64) Stanley, M. J.; Matthiesen, C.; Hansom, J.; Le Gall, C.; Schulte, C. H. H.; Clarke, E.; Atatüre, M. Dynamics of a Mesoscopic Nuclear Spin Ensemble Interacting with an Optically Driven Electron Spin. *Phys. Rev. B - Condens. Matter Mater. Phys.* **2014**.

(65) Éthier-Majcher, G.; Gangloff, D.; Stockill, R.; Clarke, E.; Hugues, M.; Le Gall, C.; Atatüre, M. Improving a Solid-State Qubit through an Engineered Mesoscopic Environment. *Phys. Rev. Lett.* **2017**.

(66) Oulton, R.; Greilich, A.; Verbin, S. Y.; Cherbunin, R. V.; Auer, T.; Yakovlev, D. R.; Bayer, M.; Merkulov, I. A.; Stavarache, V.; Reuter, D.; et al. Subsecond Spin Relaxation Times in Quantum Dots at Zero Applied Magnetic Field Due to a Strong Electron-Nuclear Interaction. *Phys. Rev. Lett.* **2007**.

(67) Heiss, D.; Schaeck, S.; Huebl, H.; Bichler, M.; Abstreiter, G.; Finley, J. J.; Bulaev, D. V.; Loss, D. Observation of Extremely Slow Hole Spin Relaxation

in Self-Assembled Quantum Dots. *Phys. Rev. B - Condens. Matter Mater. Phys.* **2007**.

(68) Gerardot, B. D.; Brunner, D.; Dalgarno, P. A.; Öhberg, P.; Seidl, S.; Kroner, M.; Karrai, K.; Stoltz, N. G.; Petroff, P. M.; Warburton, R. J. Optical Pumping of a Single Hole Spin in a Quantum Dot. *Nature* **2008**, *451* (7177), 441–444.

(69) Javadi, A.; Ding, D.; Appel, M. H.; Mahmoodian, S.; Löbl, M. C.; Söllner, I.; Schott, R.; Papon, C.; Pregnolato, T.; Stobbe, S.; et al. Spin-Photon Interface and Spin-Controlled Photon Switching in a Nanobeam Waveguide. *Nat. Nanotechnol.* **2018**.

(70) Sun, S.; Kim, H.; Solomon, G. S.; Waks, E. Cavity-Enhanced Optical Readout of a Single Solid-State Spin. *Phys. Rev. Appl.* **2018**.

(71) Zhai, L.; Löbl, M. C.; Nguyen, G. N.; Ritzmann, J.; Javadi, A.; Spinnler, C.; Wieck, A. D.; Ludwig, A.; Warburton, R. J. Low-Noise GaAs Quantum Dots for Quantum Photonics. *Nat. Commun.* **2020**.

(72) Press, D.; Ladd, T. D.; Zhang, B.; Yamamoto, Y. Complete Quantum Control of a Single Quantum Dot Spin Using Ultrafast Optical Pulses. *Nature* **2008**, *456* (7219), 218–221.

(73) Hanson, R.; Gywat, O.; Awschalom, D. D. Room-Temperature Manipulation and Decoherence of a Single Spin in Diamond. *Phys. Rev. B - Condens. Matter Mater. Phys.* **2006**.

(74) Zhong, M.; Hedges, M. P.; Ahlefeldt, R. L.; Bartholomew, J. G.; Beavan, S. E.; Wittig, S. M.; Longdell, J. J.; Sellars, M. J. Optically Addressable Nuclear Spins in a Solid with a Six-Hour Coherence Time. *Nature* **2015**.

(75) Zhong, T.; Kindem, J. M.; Miyazono, E.; Faraon, A. Nanophotonic Coherent Light-Matter Interfaces Based on Rare-Earth-Doped Crystals. *Nat. Commun.* **2015**.

(76) Hennessy, K.; Badolato, A.; Winger, M.; Gerace, D.; Atatüre, M.; Gulde, S.; Fält, S.; Hu, E. L.; Imamoğlu, A. Quantum Nature of a Strongly Coupled Single Quantum Dot–Cavity System. *Nature* **2007**, *445* (7130), 896–899.

(77) Aoki, T.; Dayan, B.; Wilcut, E.; Bowen, W. P.; Parkins, A. S.; Kippenberg, T. J.; Vahala, K. J.; Kimble, H. J. Observation of Strong Coupling between One Atom and a Monolithic Microresonator. *Nature* **2006**, *443* (7112), 671–674.

(78) Akahane, Y.; Asano, T.; Song, B. S.; Noda, S. High-Q Photonic Nanocavity in a Two-Dimensional Photonic Crystal. *Nature* **2003**.

(79) Toishi, M.; Englund, D.; Faraon, A.; Vučković, J. High-Brightness Single Photon Source from a Quantum Dot in a Directional-Emission Nanocavity. *Opt. Express* **2009**.

(80) Takagi, H.; Ota, Y.; Kumagai, N.; Ishida, S.; Iwamoto, S.; Arakawa, Y. High Q H1 Photonic Crystal Nanocavities with Efficient Vertical Emission. *Opt. Express* **2012**, *20* (27), 28292.

(81) Ates, S.; Sapienza, L.; Davanco, M.; Badolato, A.; Srinivasan, K. Bright Single-Photon Emission from a Quantum Dot in a Circular Bragg Grating Microcavity. *IEEE J. Sel. Top. Quantum Electron.* **2012**.

(82) Li, L.; Chen, E. H.; Zheng, J.; Mouradian, S. L.; Dolde, F.; Schröder, T.; Karaveli, S.; Markham, M. L.; Twitchen, D. J.; Englund, D. Efficient Photon Collection from a Nitrogen Vacancy Center in a Circular Bullseye Grating. *Nano Lett.* **2015**.

(83) Akahane, Y.; Asano, T.; Song, B.-S.; Noda, S. Fine-Tuned High-Q Photonic-Crystal Nanocavity. *Opt. Express* **2005**, *13* (4), 1202.

(84) Kim, J.-H.; Cai, T.; Richardson, C. J. K.; Leavitt, R. P.; Waks, E. Two-Photon Interference from a Bright Single-Photon Source at Telecom Wavelengths. *Optica* **2016**.

(85) Sapienza, L.; Davanço, M.; Badolato, A.; Srinivasan, K. Nanoscale Optical Positioning of Single Quantum Dots for Bright and Pure Single-Photon Emission. *Nat. Commun.* **2015**.

(86) Takagi, H.; Ota, Y.; Kumagai, N.; Ishida, S.; Iwamoto, S.; Arakawa, Y. High Q H1 Photonic Crystal Nanocavities with Efficient Vertical Emission. *Opt. Express* **2012**.

(87) Hagemeier, J.; Bonato, C.; Truong, T.-A.; Kim, H.; Beirne, G. J.; Bakker, M.; van Exter, M. P.; Luo, Y.; Petroff, P.; Bouwmeester, D. H1 Photonic Crystal Cavities for Hybrid Quantum Information Protocols. *Opt. Express* **2012**, *20* (22), 24714.

(88) Akahane, Y.; Asano, T.; Song, B.-S.; Noda, S. High-Q Photonic Nanocavity in a Two-Dimensional Photonic Crystal. *Nature* **2003**, *425* (6961), 944–947.

(89) Greilich, A.; Economou, S. E.; Spatzek, S.; Yakovlev, D. R.; Reuter, D.; Wieck, A. D.; Reinecke, T. L.; Bayer, M. Ultrafast Optical Rotations of Electron Spins in Quantum Dots. *Nat. Phys.* **2009**, *5* (4), 262–266.

(90) Atatüre, M.; Dreiser, J.; Badolato, A.; Högele, A.; Karrai, K.; Imamoglu, A. Quantum-Dot Spin-State Preparation with Near-Unity Fidelity. *Science (80-.).* **2006**, *312* (5773), 551–553.

(91) He, Y.; He, Y.-M.; Wei, Y.-J.; Jiang, X.; Chen, M.-C.; Xiong, F.-L.; Zhao, Y.; Schneider, C.; Kamp, M.; Höfling, S.; et al. Indistinguishable Tunable Single Photons Emitted by Spin-Flip Raman Transitions in InGaAs Quantum Dots. *Phys. Rev. Lett.* **2013**, *111* (23), 237403.

(92) Rakher, M. T.; Stoltz, N. G.; Coldren, L. A.; Petroff, P. M.; Bouwmeester, D. Externally Mode-Matched Cavity Quantum Electrodynamics with Charge-Tunable Quantum Dots. *Phys. Rev. Lett.* **2009**, *102* (9), 097403.

(93) Carter, S. G.; Sweeney, T. M.; Kim, M.; Kim, C. S.; Solenov, D.; Economou, S. E.; Reinecke, T. L.; Yang, L.; Bracker, A. S.; Gammon, D. Quantum Control of a Spin Qubit Coupled to a Photonic Crystal Cavity. *Nat. Photonics* **2013**, *7* (4), 329–334.

(94) Miguel-Sánchez, J.; Reinhard, A.; Togan, E.; Volz, T.; Imamoglu, A.; Besga, B.; Reichel, J.; Estève, J. Cavity Quantum Electrodynamics with Charge-Controlled Quantum Dots Coupled to a Fiber Fabry–Perot Cavity. *New J. Phys.* **2013**, *15* (4), 045002.

(95) Yoshie, T.; Scherer, A.; Hendrickson, J.; Khitrova, G.; Gibbs, H. M.; Rupper, G.; Ell, C.; Shchekin, O. B.; Deppe, D. G. Vacuum Rabi Splitting with a Single Quantum Dot in a Photonic Crystal Nanocavity. *Nature* **2004**, *432* (7014), 200–203.

(96) Reithmaier, J. P.; Sęk, G.; Löffler, A.; Hofmann, C.; Kuhn, S.; Reitzenstein, S.; Keldysh, L. V.; Kulakovskii, V. D.; Reinecke, T. L.; Forchel, A. Strong Coupling in a Single Quantum Dot–Semiconductor Microcavity System. *Nature* **2004**, *432* (7014), 197–200.

(97) Xu, X.; Wu, Y.; Sun, B.; Huang, Q.; Cheng, J.; Steel, D. G.; Bracker, A. S.; Gammon, D.; Emary, C.; Sham, L. J. Fast Spin State Initialization in a Singly Charged InAs-GaAs Quantum Dot by Optical Cooling. *Phys. Rev. Lett.* **2007**, *99* (9), 097401.

(98) Hennessy, K.; Badolato, A.; Winger, M.; Gerace, D.; Atatüre, M.; Gulde, S.; Fält, S.; Hu, E. L.; Imamoğlu, A. Quantum Nature of a Strongly Coupled Single Quantum Dot–Cavity System. *Nature* **2007**, *445* (7130), 896–899.

(99) Daveau, R. S.; Balram, K. C.; Pregnolato, T.; Liu, J.; Lee, E. H.; Song, J. D.; Verma, V.; Mirin, R.; Nam, S. W.; Midolo, L.; et al. Efficient Fiber-Coupled Single-Photon Source Based on Quantum Dots in a Photonic-Crystal Waveguide. *Optica* **2017**, *4* (2), 178.

(100) Faraon, A.; Waks, E.; Englund, D.; Fushman, I.; Vučković, J. Efficient Photonic Crystal Cavity-Waveguide Couplers. *Appl. Phys. Lett.* **2007**, *90* (7), 073102.

(101) Greuter, L.; Starosielec, S.; Najer, D.; Ludwig, A.; Duempelmann, L.; Rohner, D.; Warburton, R. J. A Small Mode Volume Tunable Microcavity: Development and Characterization. *Appl. Phys. Lett.* **2014**, *105* (12), 121105.

(102) Sun, S.; Waks, E. Deterministic Generation of Entanglement between a Quantum-Dot Spin and a Photon. *Phys. Rev. A* **2014**, *90* (4), 042322.

(103) Sun, S.; Waks, E. Single-Shot Optical Readout of a Quantum Bit Using Cavity Quantum Electrodynamics. *Phys. Rev. A* **2016**, *94* (1), 012307.

(104) Gangloff, D. A.; Éthier-Majcher, G.; Lang, C.; Denning, E. V.; Bodey, J. H.; Jackson, D. M.; Clarke, E.; Hugues, M.; Le Gall, C.; Atatüre, M. Quantum Interface of an Electron and a Nuclear Ensemble. *Science (80-.).* **2019**.

(105) Gerardot, B. D.; Brunner, D.; Dalgarno, P. A.; Öhberg, P.; Seidl, S.; Kroner, M.; Karrai, K.; Stoltz, N. G.; Petroff, P. M.; Warburton, R. J. Optical Pumping of a Single Hole Spin in a Quantum Dot. *Nature* **2008**.

(106) Bodey, J. H.; Stockill, R.; Denning, E. V.; Gangloff, D. A.; Éthier-Majcher, G.; Jackson, D. M.; Clarke, E.; Hugues, M.; Gall, C. Le; Atatüre, M. Optical Spin

Locking of a Solid-State Qubit. *npj Quantum Inf.* **2019**.

(107) Press, D.; Ladd, T. D.; Zhang, B.; Yamamoto, Y. Complete Quantum Control of a Single Quantum Dot Spin Using Ultrafast Optical Pulses. *Nature* **2008**.

(108) Kroner, M.; Weiss, K. M.; Biedermann, B.; Seidl, S.; Manus, S.; Holleitner, A. W.; Badolato, A.; Petroff, P. M.; Gerardot, B. D.; Warburton, R. J.; et al. Optical Detection of Single-Electron Spin Resonance in a Quantum Dot. *Phys. Rev. Lett.* **2008**.

(109) Stockill, R.; Le Gall, C.; Matthiesen, C.; Huthmacher, L.; Clarke, E.; Hugues, M.; Atatüre, M. Quantum Dot Spin Coherence Governed by a Strained Nuclear Environment. *Nat. Commun.* **2016**.

(110) Bluhm, H.; Foletti, S.; Neder, I.; Rudner, M.; Mahalu, D.; Umansky, V.; Yacoby, A. Dephasing Time of GaAs Electron-Spin Qubits Coupled to a Nuclear Bath Exceeding 200 Ms. *Nat. Phys.* **2011**, *7* (2), 109–113.

(111) Farfurnik, D.; Jarmola, A.; Pham, L. M.; Wang, Z. H.; Dobrovitski, V. V.; Walsworth, R. L.; Budker, D.; Bar-Gill, N. Optimizing a Dynamical Decoupling Protocol for Solid-State Electronic Spin Ensembles in Diamond. *Phys. Rev. B - Condens. Matter Mater. Phys.* **2015**.

(112) Kobel, P.; Breyer, M.; Köhl, M. Deterministic Spin-Photon Entanglement from a Trapped Ion in a Fiber Fabry–Perot Cavity. *npj Quantum Inf.* **2021**.

(113) Englund, D.; Faraon, A.; Fushman, I.; Stoltz, N.; Petroff, P.; Vučković, J. Controlling Cavity Reflectivity with a Single Quantum Dot. *Nature* **2007**, *450* (7171), 857–861.

(114) Najer, D.; Sollner, I.; Loebl, M. C.; Riedel, D.; Petrak, B.; Starosielec, S.; Dolique, V.; Valentin, S. R.; Schott, R.; Wieck, A. D.; et al. A Charge-Tunable Quantum Dot Deep in The Strong Coupling Regime of Cavity QED. In *2018 IEEE Photonics Society Summer Topical Meeting Series (SUM)*; IEEE, 2018; pp 169–170.

(115) Englund, D.; Fattal, D.; Waks, E.; Solomon, G.; Zhang, B.; Nakaoka, T.; Arakawa, Y.; Yamamoto, Y.; Vučković, J. Controlling the Spontaneous Emission Rate of Single Quantum Dots in a Two-Dimensional Photonic Crystal. *Phys. Rev. Lett.* **2005**, *95* (1), 013904.

(116) Mücke, M.; Figueroa, E.; Bochmann, J.; Hahn, C.; Murr, K.; Ritter, S.; Villas-Boas, C. J.; Rempe, G. Electromagnetically Induced Transparency with Single Atoms in a Cavity. *Nature* **2010**, *465* (7299), 755–758.